The Astrophysical Journal, 719:425–450, 2010 August 10 doi:10.1088/0004-637X/719/1/425

ULTRA-DEEP MID-INFRARED SPECTROSCOPY OF LUMINOUS INFRARED GALAXIES AT $z \sim 1$ AND $z \sim 2$

Dario Fadda[1], Lin Yan[1], Guilaine Lagache[2], Anna Sajina[3], Dieter Lutz[4], Stijn Wuyts[5,11], David T. Frayer[1], Delphine Marcillac[2], Emeric Le Floc'h[6], Karina Caputi[7], Henrik W. W. Spoon[8], Sylvain Veilleux[9], Andrew Blain[10], and George Helou[1]

[1] IPAC, California Institute of Technology, Pasadena, CA 91125, USA; fadda@ipac.caltech.edu, lyan@ipac.caltech.edu
[2] Institut d'Astrophysique Spatiale, University Paris-Sud 11 and CNRS (UMR 8617), F-91405 Orsay, France
[3] Haverford College, Haverford, PA 19041, USA
[4] Max-Planck-Institut für Extraterrestrische Physik, 85741 Garching, Germany
[5] Harvard-Smithsonian Center for Astrophysics, 60 Garden Street, Cambridge, MA 02138, USA
[6] CEA Saclay, Service d'Astrophysique, 91191 Gif-sur-Yvette, France
[7] SUPA Institute for Astronomy, University of Edinburgh, Royal Observatory, Blackford Hill, Edinburgh EH9 3HJ, UK
[8] Department of Astronomy, Cornell University, 219 Space Sciences Building, Ithaca, NY 14853, USA
[9] Department of Astronomy, University of Maryland, College Park, MD 20742, USA
[10] Astronomy Department, California Institute of Technology, Pasadena, CA 91125, USA
Received 2009 December 21; accepted 2010 June 14; published 2010 July 20

ABSTRACT

We present ultra-deep mid-infrared spectra of 48 infrared-luminous galaxies in the GOODS-south field obtained with the Infrared Spectrograph on the *Spitzer Space Telescope*. These galaxies are selected among faint infrared sources (0.14–0.5 mJy at 24 μm) in two redshift bins (0.76–1.05 and 1.75–2.4) to sample the major contributors to the cosmic infrared background at the most active epochs. We estimate redshifts for 92% of the sample using polycyclic aromatic (PAH) and Si absorption features obtaining, in particular, eight new redshifts difficult to measure from ground-based observations. Only a few of these galaxies (5% at $z \sim 1$ and 12% at $z \sim 2$) have their total infrared luminosity dominated by emission from active galactic nuclei (AGNs). The averaged mid-IR spectrum of the $z \sim 1$ luminous infrared galaxies (LIRGs) is a very good match to the averaged spectrum of local starbursts. The averaged spectrum of the $z \sim 2$ ultra-luminous infrared galaxies (ULIRGs), because of a deeper Si absorption, is better fitted by the averaged spectrum of H II-like local ULIRGs. Combining this sample with other published data, we find that 6.2 μm PAH equivalent widths (EW) reach a plateau of ~ 1 μm for $L_{24\,\mu m} \lesssim 10^{11}\,L_{\odot}$. At higher luminosities, $EW_{6.2\,\mu m}$ anti-correlates with $L_{24\,\mu m}$. Intriguingly, high-z ULIRGs and sub-millimeter galaxies (SMGs) lie above the local $EW_{6.2\,\mu m}$–$L_{24\,\mu m}$ relationship suggesting that, at a given luminosity, high-z ULIRGs have AGN contributions to their dust emission lower than those of local counterparts. A quantitative analysis of their morphology shows that most of the luminous IR galaxies have morphologies similar to those of IR-quiet galaxies at the same redshift. All $z \sim 2$ ULIRGs of our sample are IR-excess BzK galaxies and most of them have $L_{FIR}/L_{1600\,Å}$ ratios higher than those of starburst galaxies at a given UV slope. The "IR excess" is mostly due to strong 7.7 μm PAH emission and underestimation of UV dust extinction. On the basis of the AGN-powered $L_{6\,\mu m}$ continuum measured directly from the mid-IR spectra, we estimate an average intrinsic X-ray AGN luminosity of $L_{2-10\,keV} = (0.1 \pm 0.6) \times 10^{43}$ erg s^{-1}, a value substantially lower than the prediction by Daddi et al.

Key words: galaxies: evolution – galaxies: high-redshift – galaxies: starburst – infrared: galaxies

Online-only material: color figures

1. INTRODUCTION

The cosmic infrared background (CIB) detected by *COBE* (Puget et al. 1996; Fixsen et al. 1998) peaks around 200 μm with energy comparable to the optical/UV background, implying that $\sim$ 50% of the total optical/UV emission is absorbed by dust and re-radiated at mid- to far-infrared. Using stacking methods, Dole et al. (2006) quantified that the CIB emission at 70 and 160 μm is primarily produced by 24 μm sources with $S_{24\,\mu m} \sim 0.1$–0.5 mJy. At longer wavelengths, a large part of the CIB is due to faint 24 μm sources ($S_{24\,\mu m} \sim$0.06–0.3 mJy) as shown by cross-correlations with BLAST data at 350 μm (Marsden et al. 2009) and SCUBA data at 450 and 850 μm (Serjeant et al. 2008). Going from far-IR to sub-millimetric, the CIB becomes progressively dominated by more luminous and higher redshift objects (Lagache et al. 2005). Indeed, optical spectroscopy has shown that more than 70% of these sub-mJy 24 μm sources which are major contributors to the CIB lie beyond z of 0.6, with a primary peak at $z \sim 1$ and a secondary one at $z \sim 2$, consistent with the modeling of deep 24 μm number counts (Caputi et al. 2007; Le Floc'h et al. 2005; Lagache et al. 2004; Desai et al. 2007). These sub-mJy 24 μm sources correspond to luminous infrared galaxies (LIRGs, $L_{8-1000\,\mu m} \sim 10^{11}$–$10^{12}\,L_{\odot}$) at $z \sim 1$ and to ultra-luminous infrared galaxies (ULIRGs, $L_{8-1000\,\mu m} \sim 10^{12}$–$10^{13}\,L_{\odot}$) at $z \sim 2$. The evolution of the IR population at $z \sim$ 1–2 is clearly illustrated by the infrared luminosity functions at these early epochs (Le Floc'h et al. 2005; Caputi et al. 2007; Reddy et al. 2008; Magnelli et al. 2009). In essence, the knee of the luminosity function, which marks the dominant contributors to the energy density, moves to higher luminosity with redshift: from $L_{IR} \sim$ (3–5) $\times 10^{11}\,L_{\odot}$ at $z \sim 1$ to (3–5) $\times 10^{12}\,L_{\odot}$ at $z \sim 2$. As shown by published studies (see, e.g., Le Floc'h et al. 2005), $z \sim 1$ LIRGs are responsible for 70% $\pm$ 15% of the total (UV+IR) luminosity density, and, at $z \gtrsim 1$, the contribution of ULIRGs becomes increasingly dominant.

[11] W. M. Keck Postdoctoral Fellow

While deep 24 μm surveys have revealed LIRGs and ULIRGs as primary contributors to the global energy production at early epochs, the fraction of their bolometric luminosity contaminated by active galactic nucleus (AGN) emission is not well determined. Standard multi-wavelength criteria can be used (using X-ray emission, optical spectroscopy, IRAC photometry) but none of them is able to determine the relative AGN and starburst contributions to the bolometric luminosity of IR-luminous galaxies (which is mostly equal to the 3–1000 μm luminosity). As of today, a very efficient way to probe dust obscured AGN emission is via deep mid-IR spectroscopy. The difference between the mid-IR spectra of a starburst and an AGN is striking. Starbursts are often characterized by strong, low-excitation, fine-structure lines, prominent polycyclic aromatic (PAH) features, and a weak 10 μm continuum, whereas AGNs display weak or no PAH features, plus a strong mid-infrared continuum (see, e.g., Voit 1992). Mid-IR spectroscopic surveys have thus been conducted on a number of low to high redshift samples of IR-luminous galaxies with the *Spitzer*/IRS (Armus et al. 2007; Yan et al. 2007; Sajina et al. 2008; Farrah et al. 2008; Valiante et al. 2007; Spoon et al. 2007; Weedman et al. 2006; Murphy et al. 2009; Veilleux et al. 2009). However, these samples are limited to the bright end of the IR luminosity function. Previous deep mid-IR spectroscopic observations have been attempted at the faint 24 μm flux level of 0.1–0.5 mJy, but the number of observed sources is very small (Teplitz et al. 2007; Bertincourt et al. 2009). To directly determine the AGN fraction at the lowest IR luminosity possible, we carried out an observational program to obtain low-resolution, mid-IR spectra of 48 galaxies—24 at $z \sim 1$ and 24 at $z \sim 2$—with 24 μm flux densities $\sim$0.1–0.5 mJy. The main scientific goal of this study is to provide the first observational data to characterize the spectral properties of LIRGs and ULIRGs that are responsible for the bulk on the CIB and output energy at high redshifts ($z \sim 0.7$–2.5). Combining our deep mid-IR spectra with the available optical and near-IR data in CDFS, we compare global properties such as colors, morphologies, and stellar masses of our sample galaxies with those of optically selected galaxies to provide observational constraints on the mid-IR properties of optically selected IR faint galaxies at $z \sim 1$–2.

Throughout the paper, we adopt $\Omega_M = 0.27$, $\Omega_\Lambda = 0.73$, and $H_0 = 71\,\mathrm{km\,s^{-1}\,Mpc^{-1}}$ cosmology.

2. DATA SAMPLE

2.1. Sample Selection

LIRGs and ULIRGs are responsible for most of the integrated infrared background. To study these two populations of galaxies, we selected two samples of 24 μm sources fainter than 0.5 mJy in two redshift bins (0.76–1.05 and 1.75–2.2). In these two redshift bins, the 24 μm fluxes translate to infrared luminosities roughly in the ranges for LIRGs at $z \sim 1$ and ULIRGs at $z \sim 2$. This sample is therefore crudely luminosity selected and we do not apply any other selections. The flux lower limit ($\sim$0.2 mJy) is dictated by the sensitivity of the *Spitzer* Infrared Spectrograph (IRS; Houck et al. 2004), as demonstrated by the IRS instrument support team (Teplitz et al. 2007). These targets were selected mostly using photometric redshifts computed by Caputi et al. (2006) since only 50% and 10% of them had spectroscopic-z in the $z \sim$ 1 and 2 bins, respectively. We note that all sources but two are actually in the chosen redshift bins, as confirmed by their mid-IR spectroscopic redshifts (see Section 4.2). Our 48 galaxies were selected in the Chandra Deep Field South (CDFS)

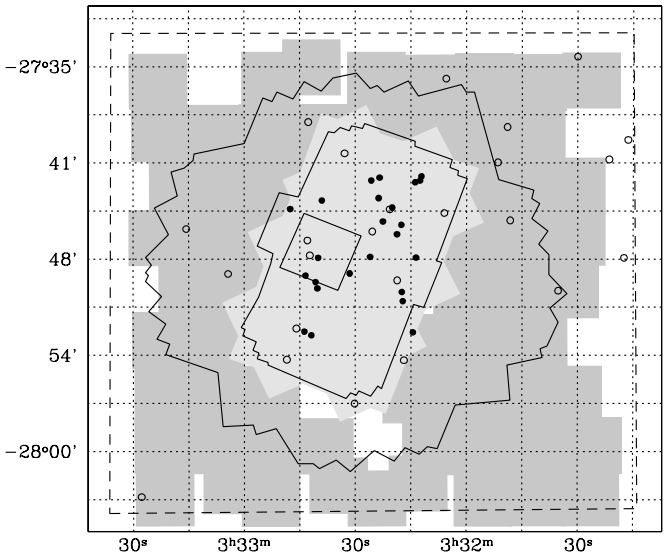

Figure 1. IRS targets overlapped on ACS images from GOODS (light gray shaded) and GEMS (gray shaded). Open and filled circles mark the $z \sim 1$ and $z \sim 2$ samples, respectively. The two internal contours mark the border of the 16 μm imaging (deep and ultra-deep observations). The external solid contour shows the coverage of deep *Chandra* imaging (Luo et al. 2008), while the external dashed contour marks the field covered by COMBO17 (Wolf et al. 2004).

Table 1
Cross-correlation with X-ray Survey

Name	Distance	Flux [10^{-16} erg s^{-1} cm^{-2}]			$L_{2-8\,\mathrm{keV}}$
	(arcsec)	(0.5–8 keV)	(0.5–2 keV)	(2–8 keV)	[10^{43}erg s^{-1}]
Primary catalog					
U428	0.29	0.76	0.35	<1.26	<0.27
U4642	0.12	2.05	0.74	1.41	0.35
U4950	0.18	60.90	13.00	47.00	18.9
U5775	0.48	<0.97	0.42	<2.39	<0.35
U5877	0.18	36.40	0.73	36.40	9.1
Secondary catalog					
L5420	0.40	<2.07	0.63	<2.91	<0.18

for which a large sample of public ancillary data is available. The selected ULIRGs are *all* the 24 μm sources in the CDFS GOODS area with $S(24\,\mu\mathrm{m}) \sim 0.14$–0.55 mJy at $z = 1.75$–2.4, excluding three sources too close to a neighbor source to obtain unblended spectra. The LIRGs have been selected among 24 μm sources with $S(24\,\mu\mathrm{m}) \sim$ 0.2–0.5 mJy at $z =$ 0.76–1.05 in order to avoid a large-scale structure localized at $z = 0.734$ (Szokoly et al. 2004). To have a more representative sample of LIRGs, spanning different luminosities within the LIRG range, we included in our selection sources from the "extended CDFS" area. The spatial distribution of the targets relative to the available Advanced Camera for Surveys (ACS) images is shown in Figure 1. Table 1 lists the sources of our sample with X-ray counterparts. Tables 2 and 3 list the 48 targets with J2000 coordinates, on-target integration times for various slit modules, 8, 16, 24, and 70 μm flux densities, and redshifts.

One important question, which is also the basic driver of this program, is how representative our sample is at the two redshift slices. Figure 2 quantitatively illustrates that our targets represent populations of infrared luminous galaxies which are energetically important in comparison with other sources. We plot the contribution of 24 μm sources to the co-moving monochromatic 12 μm and 8 μm luminosity density per logarithmic luminosity interval as a function of luminosity at

Table 2
The Sample Targets and IRS Observation Log

ID	IAU ID	R.A. (J2000)	Decl. (J2000)	SL[a] 1st	LL[a] 2nd (s × repeats)	LL[a] 1st
U428	SST24 J03:32:43.45-27:49:01.8	3:32:43.450	−27:49:01.82	0	120 × 6	120 × 9
U4367	SST24 J03:32:43.78-27:52:31.0	3:32:43.781	−27:52:31.07	0	120 × 15	120 × 22
U4451	SST24 J03:32:14.46-27:52:33.7	3:32:14.465	−27:52:33.77	0	120 × 15	120 × 22
U4499	SST24 J03:32:17.19-27:50:37.1	3:32:17.190	−27:50:37.10	0	120 × 15	120 × 22
U4631	SST24 J03:32:40.24-27:49:49.6	3:32:40.243	−27:49:49.64	0	120 × 9	120 × 13
U4639	SST24 J03:32:40.75-27:49:25.8	3:32:40.756	−27:49:25.87	0	120 × 15	120 × 22
U4642	SST24 J03:32:31.52-27:48:53.7	3:32:31.529	−27:48:53.72	0	120 × 9	120 × 13
U4812	SST24 J03:32:47.58-27:44:52.3	3:32:47.585	−27:44:52.31	0	120 × 6	120 × 9
U4950	SST24 J03:32:25.68-27:43:05.6	3:32:25.683	−27:43:05.65	0	120 × 3	120 × 5
U4958	SST24 J03:32:23.43-27:42:55.0	3:32:23.436	−27:42:55.03	0	120 × 9	120 × 13
U5050	SST24 J03:32:39.03-27:44:20.4	3:32:39.034	−27:44:20.46	0	120 × 15	120 × 22
U5059	SST24 J03:32:23.71-27:44:11.6	3:32:23.714	−27:44:11.69	0	120 × 9	120 × 13
U5150	SST24 J03:32:13.87-27:43:12.3	3:32:13.877	−27:43:12.35	0	120 × 6	120 × 9
U5152	SST24 J03:32:12.54-27:43:05.9	3:32:12.543	−27:43:05.99	0	120 × 6	120 × 9
U5153	SST24 J03:32:12.15-27:42:49.9	3:32:12.150	−27:42:49.94	0	120 × 15	120 × 22
U5632	SST24 J03:32:40.05-27:47:55.1	3:32:40.051	−27:47:55.11	0	120 × 6	60 × 16
U5652	SST24 J03:32:17.44-27:50:03.1	3:32:17.444	−27:50:03.12	0	120 × 6	60 × 16
U5775	SST24 J03:32:26.01-27:47:51.5	3:32:26.011	−27:47:51.56	0	120 × 15	120 × 22
U5795	SST24 J03:32:18.75-27:46:26.9	3:32:18.750	−27:46:26.90	0	120 × 6	120 × 9
U5801	SST24 J03:32:17.58-27:45:51.7	3:32:17.587	−27:45:51.78	0	120 × 15	120 × 22
U5805	SST24 J03:32:22.56-27:45:39.0	3:32:22.561	−27:45:39.00	0	120 × 15	120 × 22
U5829	SST24 J03:32:13.62-27:47:53.9	3:32:13.628	−27:47:53.97	0	120 × 15	120 × 22
U5877	SST24 J03:32:20.04-27:44:47.2	3:32:20.049	−27:44:47.20	0	120 × 6	120 × 14
U16526	SST24 J03:32:41.87-27:52:45.0	3:32:41.870	−27:52:45.06	0	120 × 6	120 × 9
L3832	SST24 J03:32:30.18-27:57:00.7	3:32:30.189	−27:57:00.75	60 × 32	120 × 14	0
L3945	SST24 J03:33:04.38-27:48:55.5	3:33:04.381	−27:48:55.50	60 × 32	120 × 14	0
L4020	SST24 J03:33:15.65-27:46:07.5	3:33:15.655	−27:46:07.57	60 × 32	120 × 14	0
L4177	SST24 J03:32:48.48-27:54:16.0	3:32:48.489	−27:54:16.04	60 × 32	120 × 14	0
L4419	SST24 J03:32:16.87-27:54:18.4	3:32:16.871	−27:54:18.43	60 × 32	120 × 14	0
L4900	SST24 J03:32:32.88-27:41:24.1	3:32:32.886	−27:41:24.12	60 × 32	120 × 14	0
L5134	SST24 J03:32:42.96-27:46:50.0	3:32:42.962	−27:46:50.05	60 × 32	120 × 14	0
L5367	SST24 J03:31:35.23-27:49:58.4	3:31:35.237	−27:49:58.41	60 × 32	120 × 14	0
L5420	SST24 J03:32:05.99-27:45:07.3	3:32:05.990	−27:45:07.36	60 × 16	60 × 16	0
L5511	SST24 J03:31:48.19-27:45:34.9	3:31:48.191	−27:45:34.91	60 × 16	60 × 16	0
L5630	SST24 J03:32:42.28-27:47:45.9	3:32:42.287	−27:47:45.99	60 × 32	120 × 14	0
L5659	SST24 J03:32:18.70-27:49:19.5	3:32:18.701	−27:49:19.55	60 × 32	120 × 14	0
L5876	SST24 J03:32:20.71-27:44:53.5	3:32:20.714	−27:44:53.53	60 × 32	120 × 14	0
L6211	SST24 J03:32:42.70-27:39:27.1	3:32:42.708	−27:39:27.10	120 × 6	120 × 5	0
L6221	SST24 J03:31:17.46-27:47:55.0	3:31:17.463	−27:47:55.09	60 × 32	120 × 14	0
L6473	SST24 J03:31:49.02-27:39:45.1	3:31:49.026	−27:39:45.19	120 × 6	120 × 5	0
L6658	SST24 J03:32:05.48-27:36:43.9	3:32:05.486	−27:36:43.96	120 × 6	120 × 5	0
L7079	SST24 J03:31:21.47-27:41:47.0	3:31:21.474	−27:41:47.05	60 × 32	120 × 14	0
L13667	SST24 J03:33:27.79-28:02:50.9	3:33:27.794	−28:02:50.90	120 × 6	120 × 5	0
L13958	SST24 J03:32:25.41-27:46:16.8	3:32:25.412	−27:46:16.81	60 × 16	60 × 16	0
L14143	SST24 J03:31:16.36-27:40:33.5	3:31:16.365	−27:40:33.57	60 × 16	60 × 16	0
L14228	SST24 J03:31:29.99-27:35:22.0	3:31:29.999	−27:35:22.04	60 × 32	120 × 14	0
L15906	SST24 J03:32:45.91-27:52:19.6	3:32:45.914	−27:52:19.64	60 × 32	120 × 14	0
L16005	SST24 J03:31:51.50-27:41:57.1	3:31:51.505	−27:41:57.16	60 × 32	120 × 14	0

Notes.
[a] SL and LL stand for short-low and long-low modules. SL first order, LL second order, and LL first order cover the ranges 7–14 μm, 14–21 μm, and 21–35 μm, respectively.

$z \sim 1$ and 2, respectively. Each of our targets is marked on the luminosity scale with a dashed line. The integrated comoving luminosity density is computed using both model (line; Lagache et al. 2004) and previously published, measured infrared luminosity functions (Caputi et al. 2007; Le Floc'h et al. 2005; Magnelli et al. 2009; Reddy et al. 2008). It is interesting to note that at $z \sim 1$, the combined luminosity functions independently derived by three different groups suggest that the infrared luminosity density turns over around $L_{12\,\mu\mathrm{m}} \sim 10^{10.7}\,L_{\odot}$ (Le Floc'h et al. 2005; Caputi et al. 2007; Magnelli et al. 2009). Although knowledge of the IR luminosity function is still poor at $z \sim 2$, particularly at low luminosities, the critical luminosity range $L_{8\,\mu\mathrm{m}} \sim 10^{11}$–$10^{11.5}\,L_{\odot}$ is fairly clearly highlighted in the right panel of Figure 2. We conclude that our targets indeed probe the infrared populations which dominate the energy productions at these two cosmic epochs.

Except for having higher dust obscuration, our sample galaxies do not have extremely deviant properties in the rest-frame UV/optical in comparison with galaxies selected at observed

Table 3
The Sample Target Fluxes and Redshifts

ID	$S_{8\,\mu m}$		$S_{16\,\mu m}$		$S_{24\,\mu m}$		$S_{70\,\mu m}$		z_{IRS}	z_{opt}	*	$\log(L_{24\,\mu m})$	M_*	$EW_{6.2\,\mu m}$
	(μJy)	SN	(μJy)	SN	(μJy)	SN	(*m*Jy)	SN				($L_\odot$)	($10^{10}\,M_\odot$)	(μm)
U428	15.9	68	65	24	287	38	2.43	3	1.783	(1.664)	a	11.47	4.09	1.39 ± 0.34
U4367	22.2	79	101	12	169	20	<1.55		1.624	(1.762)	a	11.23	13.10	0.54 ± 0.23
U4451	11.1	38			225	28	<1.53		1.875	(1.684)	a	11.40	3.47	0.83 ± 0.50
U4499	16.3	77	<35		182	23	<1.45		1.956	(1.909)	a	11.58	11.90	>0.84
U4631	15.4	60	<21		269	33	<1.40		1.841	1.896	1	11.39	9.61	>0.92
U4639	13.5	57	<14		216	27	<1.45		2.112	2.130	5	11.58	3.57	>2.61
U4642	12.3	60	65	7	268	32	2.14	3	1.898	(1.748)	a	11.82	2.50	1.33 ± 0.41
U4812	15.9	42	<53		317	41	3.75	13	1.930	1.910	1	12.00	6.63	>1.04
U4950	163.3	598	453	54	547	67	<1.68		2.312	2.291	4	11.79	10.41	0.12 ± 0.06
U4958	16.4	62	109	11	262	33	<1.67		2.118	2.145	5	11.51	8.50	
U5050	24.6	97	51	7	194	22	<1.50		1.938	(1.726)	a	11.40	18.93	0.60 ± 0.34
U5059	18.1	64	<37		253	31	<1.53		1.769	(1.543)	a	11.49	6.59	>1.61
U5150	13.1	35	65	6	286	37	2.98	12	1.898	(1.738)	a	11.92	2.17	0.77 ± 0.47
U5152	13.1	43	66	7	305	38	<1.77		1.794	(1.888)	a	11.44	2.75	0.50 ± 0.34
U5153	19.2	68	<34		183	21	<1.71		2.442	(2.030)	b	11.73		>0.41
U5632	19.2	86	83	35	421	52	<1.38		2.016	1.998	1	11.75	6.79	0.99 ± 0.22
U5652	30.3	153	154	17	316	44	3.24	8	1.618	1.616	1	11.68	15.73	1.21 ± 0.23
U5775	9.6	51	<31		141	16	2.64	11	1.897	(1.779)	a	11.61	5.30	>0.72
U5795	18.7	63	<31		264	33	<1.43		1.703	(1.524)	a	11.36	5.63	>2.16
U5801	16.2	57	<35		216	24	<1.45		1.841	(1.642)	a	11.25	13.68	>0.83
U5805	8.0	25	68	11	170	19	<1.45		2.073	(2.093)	a	11.74	1.16	0.41 ± 0.18
U5829	15.4	69	57	12	208	26	<1.40		1.742	(1.597)	a	11.32	9.21	0.98 ± 0.31
U5877	31.7	120	179	23	360	48	3.88	19	1.886	(1.708)	a	11.77	3.54	0.17 ± 0.10
U16526	20.6	66	69	18	306	45	5.17	13	1.749	(1.718)	a	12.00	4.05	0.53 ± 0.35
L3832	23.5	61			207	28	<1.90		0.767	(0.763)	b	10.53	4.39	0.81 ± 0.46
L3945	19.0	18			367	39	3.81	11		(0.950)	b	11.08	0.37	0.20 ± 0.05
L4020	20.8	30			332	38	4.22	21	0.826	(0.779)	b	10.90	3.10	1.13 ± 0.13
L4177	20.5	70	204	22	208	27	<1.78		0.842	0.840	3	10.62	3.71	0.91 ± 0.26
L4419	46.8	159			259	38	4.06	13	0.974	(0.995)	b	11.08	11.23	0.46 ± 0.23
L4900	26.8	95	267	32	213	31	<1.82		1.047	1.045	5	10.91	6.75	1.11 ± 0.05
L5134	22.6	106	269	110	229	28	<1.42		1.039	1.036	1	10.84	5.02	1.04 ± 0.32
L5367	24.3	27			252	26	<1.92		0.974	(0.868)	b	10.86	5.79	1.06 ± 0.07
L5420	36.7	135	450	48	381	46	2.76	5	1.068	1.068	3	11.15	4.42	0.91 ± 0.20
L5511	38.6	50			401	54	2.22	5		(2.08)	c	11.87	25.90	0.48 ± 0.23
L5630	22.8	104	277	149	286	36	2.06	3	0.997	0.996	3	10.93	2.27	1.24 ± 0.16
L5659	28.6	129	285	25	231	30	2.41	9	1.044	1.038	1	11.00	4.57	1.13 ± 0.53
L5876	29.2	103	310	41	330	43	2.54	15	0.971	0.969	1	10.98	7.16	1.11 ± 0.04
L6211	31.5	84			457	62	<1.88		1.843	(1.840)	c	11.70		1.56 ± 0.22
L6221	19.1	14			239	12	<2.87		1.012	(0.989)	b	11.02		1.04 ± 0.26
L6473	32.3	44			484	63	2.78	8	0.816	0.811	1	10.83		1.10 ± 0.28
L6658	45.2	60			467	59	<1.87		0.969	(0.963)	b	10.94	12.54	1.33 ± 0.24
L7079	23.3	20			289	27	3.21	8	0.955	(0.884)	b	11.00		1.01 ± 0.01
L13667	33.8	30			496	64	<2.65		0.936	(0.924)	b	11.00		1.57 ± 0.01
L13958	21.8	83	292	39	376	47	3.31	13	0.891	0.896	2	10.96	2.10	1.99 ± 0.24
L14143	34.8	22			427	35	4.71	8	1.043	(0.965)	b	11.29		0.89 ± 0.08
L14228	23.8	23			313	35	<2.12		0.953	(0.961)	b	10.89	3.02	1.55 ± 0.21
L15906	18.4	63	193	23	262	41	3.23	8	0.976	(1.045)	a	11.02	0.44	1.13 ± 0.17
L16005	24.2	32			253	42	3.29	9	0.865	(0.984)	b	10.86	1.59	1.60 ± 0.06

Notes. *Spectroscopic redshifts from (1) Vanzella et al. 2006, 2008; (2) Mignoli et al. 2005; (3) Le Fèvre et al. 2004; (4) Szokoly et al. 2004; (5) Popesso et al. 2009; photometric redshifts from (a) Wuyts et al. 2008; (b) Caputi et al. 2004; (c) this paper.

optical/near-IR band. For example, Section 4.7 discusses in detail that the observed optical/near-IR colors of our sources are very similar to those of extremely red galaxy (ERG) populations selected by large area *K*-band surveys. Figure 3 shows the most recently published stellar mass functions for redshift slices of 0.8–1.0 (black lines and circles) and 1.5–2.0 (red lines and circles) by Ilbert et al. (2010), and the dashed, vertical lines mark the estimated stellar masses for the galaxies in our sample. The method used to derive the stellar masses is described in Wuyts et al. (2009b). It assumes a Kroupa's initial mass function (Kroupa 2001), stellar population synthesis models by Bruzual & Charlot (2003), and the reddening law of Calzetti et al. (2000). The same set of assumptions is also used by Ilbert et al. (2010). This figure clearly illustrates that our $z \sim 1$ LIRGs mostly have stellar masses near or a bit lower than M^*, the turnover of the mass function, thus probing the most representative and important mass scales at this redshift slice. The $z \sim 2$ ULIRGs reaches much lower masses, $\lesssim 10^{11}\,M_\odot$, than those published in Ilbert et al. (2010) using COSMOS data. This is because the complete catalog used to construct these mass functions is cut

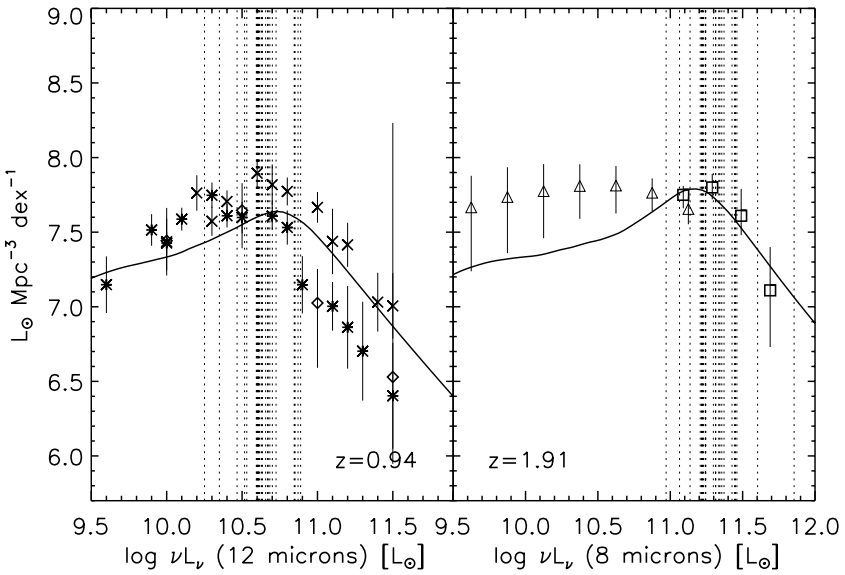

Figure 2. Co-moving 12 and 8 μm energy output per dex of 12 and 8 μm luminosity ($L\,dN/d\log L$) at $z = 0.94$ and $z = 1.91$, corresponding to the mean redshifts of our two bins. Continuous lines are from the model of Lagache et al. (2004). Diamonds, squares, and triangles are from Le Floc'h et al. (2005), Caputi et al. (2007), and Reddy et al. (2008), respectively. At $z \sim 1$, stars and crosses are derived using the $0.7 < z < 1$ and $1 < z < 1.3$ 15 μm luminosity functions from Magnelli et al. (2009). Dotted lines represent the rest-frame 12 and 8 μm luminosities of our 48 targets computed from their 24 μm fluxes. No color correction has been applied.

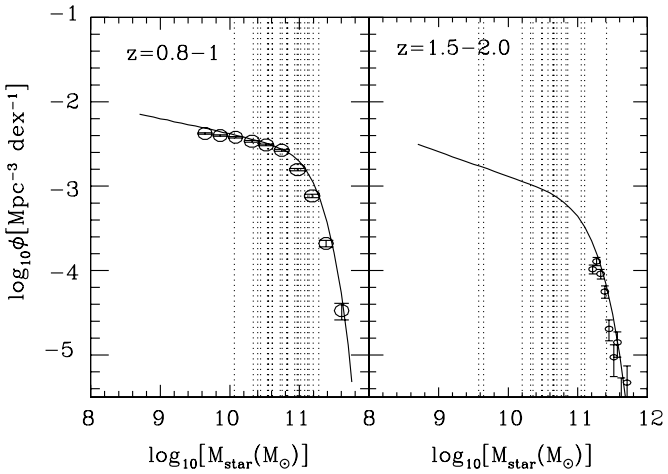

Figure 3. Stellar mass functions at $z \sim 1$–2 published by Ilbert et al. (2010) using the COSMOS data. The dashed lines mark the stellar masses of our sources estimated as in Wuyts et al. (2009b).

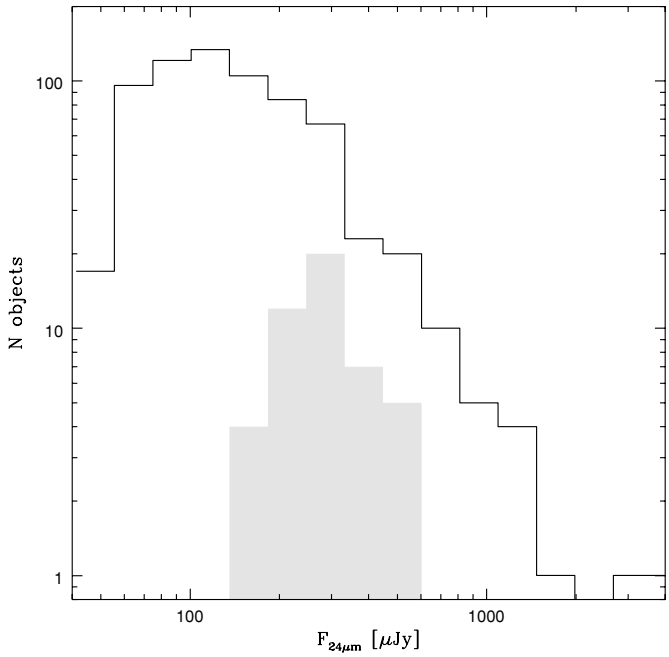

Figure 4. 24 μm fluxes of our IRS targets (shaded histogram) compared with the flux distribution of all the 24 μm sources in the GOODS–CDFS field (solid histogram).

at $i_{AB} \lesssim 25.5$. This suggests that many of our $z \sim 2$ ULIRGs have fainter optical magnitudes ($i_{AB} > 25.5$).

2.2. IRS Observations and Ancillary Data

As shown in Figure 4, our targets have 24 μm fluxes of 0.14–0.55 mJy in comparison with the distribution of all 24 μm galaxies within the GOODS-south field (approximately 0.05 deg^2). For these ultra-deep, low resolution observations, we use the IRS in mapping mode, with four dithered positions along the slit for each target. All observations were scheduled during each campaign just after the dark calibration observations. This method has been shown to be effective in reducing potential latencies left by previous observations of bright sources (Teplitz et al. 2007). Our IRS spectra will sample important PAH features at 6.2 μm and 7.7 μm, with the observed coverage of 7–21 μm for LIRGs and the 14–35 μm range for ULIRGs.

The CDFS field is remarkable for the great amount of ancillary data publicly available. In this paper, we make use of this rich dataset, including *Chandra* X-ray data, deep *Hubble Space Telescope* (*HST*) images at optical/UV, ground-based near-IR data, and the *Spitzer* images taken with MIPS (24 μm and 70 μm), IRS (16 μm), and IRAC (8.0 μm). We reduced the *Spitzer* data by ourselves, and directly took the reduced *HST* images from the GOODS (Giavalisco et al. 2004) and GEMS surveys (Rix et al. 2004), as well as the recent FIREWORKS (Wuyts et al. 2008) and MUSYC[12] multi-wavelength photometric catalogs (Gawiser et al. 2006). Most of the sources of our IRS sample are covered by the 2 Ms CDFS Survey (Luo et al.

[12] http://www.strw.leidenuniv.nl/fireworks, http://www.astro.yale.edu/MUSYC/

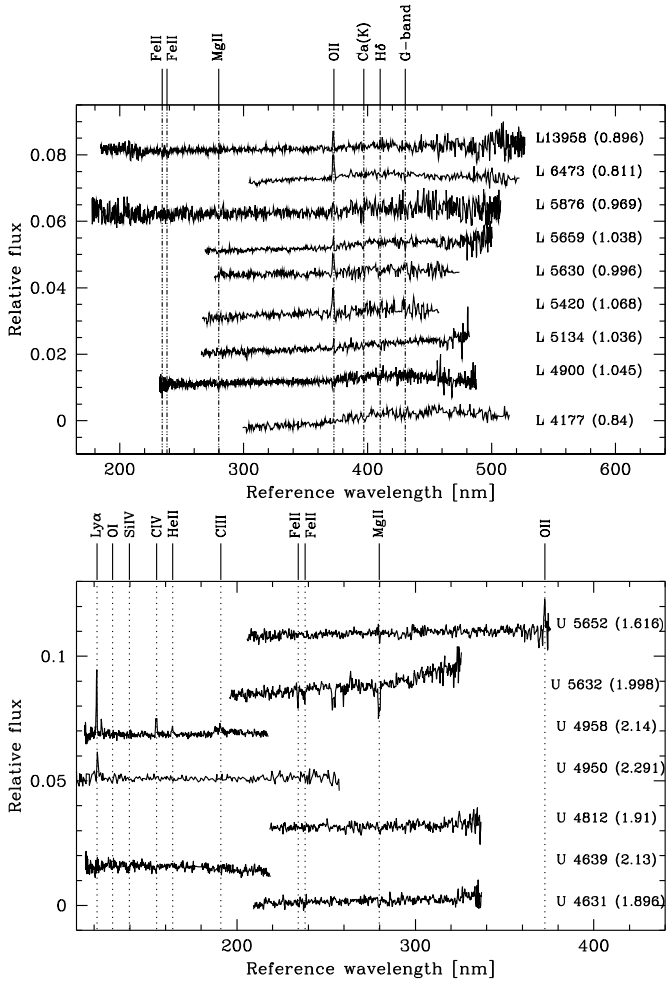

Figure 5. Optical spectra available for LIRGs (top) and ULIRGs (bottom) of our sample. The main absorption and emission features are marked. Estimated optical redshifts are reported between brackets.

2008, see Figure 1). We use the X-ray catalog from Luo et al. (2008) for our analysis in Section 4.3.

2.3. Optical Spectra

Published optical spectra exist for 17 ULIRGs and nine LIRGs of our sample. The redshift estimate is usually easy for the $z \sim 1$ sample because of the large number of features in the spectra ([O III], Ca, *G* band) and becomes more complex in the case of $z \sim 2$ sources. In fact, there are good optical spec-z estimates for nine LIRGs while only seven ULIRGs have optical spectra with enough features to give reliable redshifts (see Table 3). Remarkably, all these spectra are available as FITS files and we were able to inspect each of them and confirm or correct the redshift estimates of the original publications. In the case of L4900, the published $z_{\rm spec}$(opt) of 0.978 (Popesso et al. 2009) was revised to 1.045 which is now perfectly consistent with the estimate derived from the IRS spectrum. All the spectra with good redshift estimates (according to the published references) are reported in Figure 5. The only exception is the spectrum of U5795 (from Mignoli et al. 2005) whose FITS file is corrupted. The published optical redshift is not reported in Table 3 since we were not able to confirm it. On the other hand, we include the spectrum of U4631 in the figure and the table although it has been classified as unsure since it has clear Mg II and Fe II lines and its optical spec-z is similar to that estimated from the mid-IR spectrum. The optical spectral lines will be used in the discussion on the AGN fraction in Section 4.3.

3. MID-IR DATA REDUCTION

The reduction of the IRS data was carried out with a new software written by the first author specifically for low-resolution IRS spectra. A detailed description of the technique used is given in the Appendix.

We reduced and measured fluxes of our targets in the 8 μm IRAC, 16 μm IRS, and 24 and 70 μm MIPS images. For the IRAC data, we started from the *Spitzer* basic calibrated data (BCDs) applying artifact corrections before mosaicking. The artifact corrections include column pull-downs, muxbleed, optical banding, and background droops. We mosaicked the image with MOPEX with a pixel size of 0.″6. The photometry within an aperture of 3.″8 in radius was measured using SExtractor (Bertin & Arnouts 1996). The final IRAC 8 μm flux was computed using a flux conversion factor of 0.2021 MJy/sr/(DN/s), and aperture corrections of 1.84 (see SWIRE technical report,[13] p. 31). For the IRS 16 μm images, we obtained a superflat by stacking the original BCDs. Each BCD is then corrected with this superflat. Because we are only interested in point sources, we subtracted the median background from each BCD before mosaicking them with MOPEX with a 0.″9 pixel. We extracted the sources using point-spread function (PSF) fitting with the code StarFinder (Diolaiti et al. 2000) inside an aperture of 9.″45 and applied an aperture correction of 1.1626 (computed with a theoretical PSF obtained with STinyTim[14]). The flux conversion used is 0.0117 MJy sr^{-1} (DN/s)$^{-1}$. In case no counterpart was found, we also computed 5σ flux upper limits.

The 24 μm image was reduced using an improved version of the method described in Fadda et al. (2006), which now corrects the long-term transient and the regular short-term baseline variations. The long term is treated as a multiplicative effect since it has been proved in the case of MIPS 70 and 160 μm, for which we have an internal calibration, that it is due to a variation in the responsivity of the detector. The short-term regular variation of the baseline is due to distortions introduced by the different positions of the cryogenic mirror assumed to freeze the image during a scan. This variation is corrected by taking into account these distortions. We made the mosaic image with MOPEX and extracted sources using StarFinder with an aperture of 14″, and applying the aperture and color correction of 1.158 and 0.961, respectively (Fadda et al. 2006).[15] The flux conversion is 0.0454 MJy sr^{-1} (DN/s)$^{-1}$.

Finally, the 70 μm imaging data are the deepest available, from the Far-infrared Deep Extragalactic Legacy Survey.[16] We start our reduction from the raw data using the off-line *Spitzer* software (GeRT[17]). The pipeline corrects the calibration drifts, nonlinearity, and latencies due to stimflashes, and applies the flux conversion before computing the slopes of the ramps. We remove any streaking in the final images by using filtering on the first-pass images with bright sources masked out. The final mosaic with a pixel size of 4″ was obtained with MOPEX and sources were extracted with StarFinder with an aperture of 42″ in diameter. We apply the aperture correction of 1.1665

[13] http://swire.ipac.caltech.edu/swire/astronomers/publications
[14] http://ssc.spitzer.caltech.edu/archanaly/contributed/stinytim
[15] The MIPS photometric system is tied to spectra with constant νf_ν, see MIPS data handbook, http://ssc.spitzer.caltech.edu/mips/dh, p. 31.
[16] http://ssc.spitzer.caltech.edu/legacy/all.html
[17] http://ssc.spitzer.caltech.edu/mips/gert

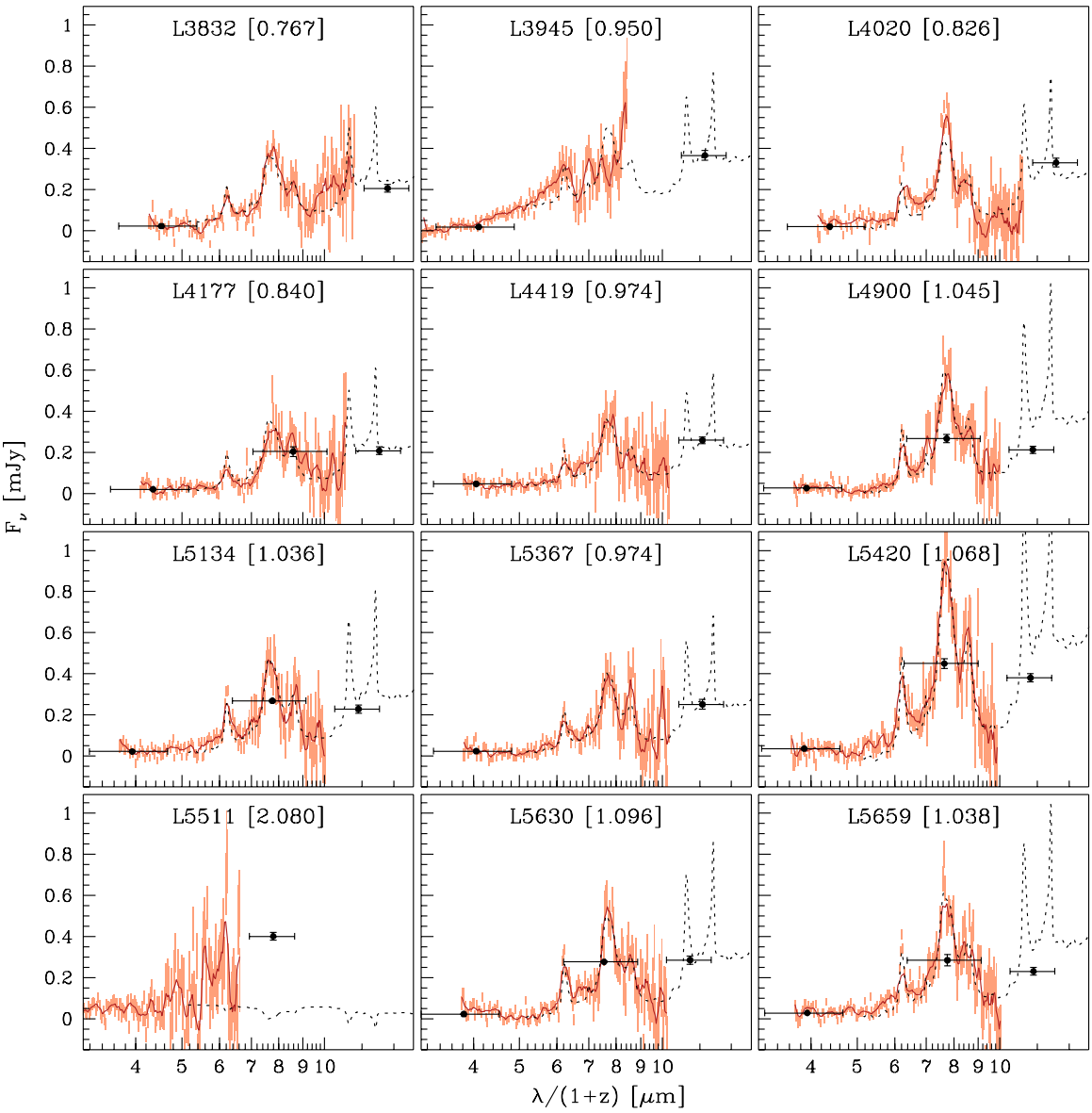

Figure 6. Observed spectra for our sample of 24 LIRGs. The solid line, corresponding to the data with a smoothing of 5 pixels, is on the top of the shaded 1σ error bars for each pixel. Broadband fluxes are overplotted. Dotted lines are either the averaged local starburst template from Brandl et al. (2006) or the hot dust dominated spectrum from Spoon et al. (2007) rescaled to the data. Source names and redshifts appear on the top of each panel.

(A color version of this figure is available in the online journal.)

(computed with STinyTim) and a color correction of 0.918 to tie the photometric system to spectra with constant νf_ν. The flux conversion is 702 MJy sr^{-1} (DN/s)$^{-1}$. In case no counterpart was found, we also computed 5σ flux upper limits. The fluxes in these bands are reported in Table 3 and in Figures 6, 7, and 13. The flux limits in these two figures are in 5σ for all bands. All the flux conversion factors reported are the conversion factors applied by the *Spitzer* pipeline used at the time of our data reduction. We report these factors, as well as the aperture corrections used, to allow a comparison with older or future reduction of other *Spitzer* data.

4. RESULTS

4.1. Observed Mid-IR Spectra

Figures 6 and 7 present the observed mid-IR spectra for the 24 LIRGs at $z \sim 1$ and 24 ULIRGs at $z \sim 2$. In each panel, the smoothed spectrum in the rest-frame wavelength is shown as a red solid line, a local spectral template as a dashed line, and the unsmoothed spectrum with error bars as an orange histogram. Each panel indicates the broadband fluxes at 8 μm, 16 μm, and 24 μm, the object name, the redshift based on the mid-IR spectrum, or optical redshifts when the mid-IR spectra do not yield redshifts (which is only the case for three LIRGs). Downward arrows mark 5σ flux upper limits. The spectral template shown in the dashed line in each panel is either the averaged starburst spectrum obtained by Brandl et al. (2006) based on the *Spitzer* spectra of 22 local starburst galaxies, or the AGN template 1A (Spoon et al. 2007) if the observed spectrum has no obvious PAH emission. Redshifts are estimated from the mid-IR spectra by cross-correlating these two templates to the data. In Figures 6 and 7, the overlapped local spectral templates allow a simple characterization of the observed spectra of our high-z LIRGs and ULIRGs.

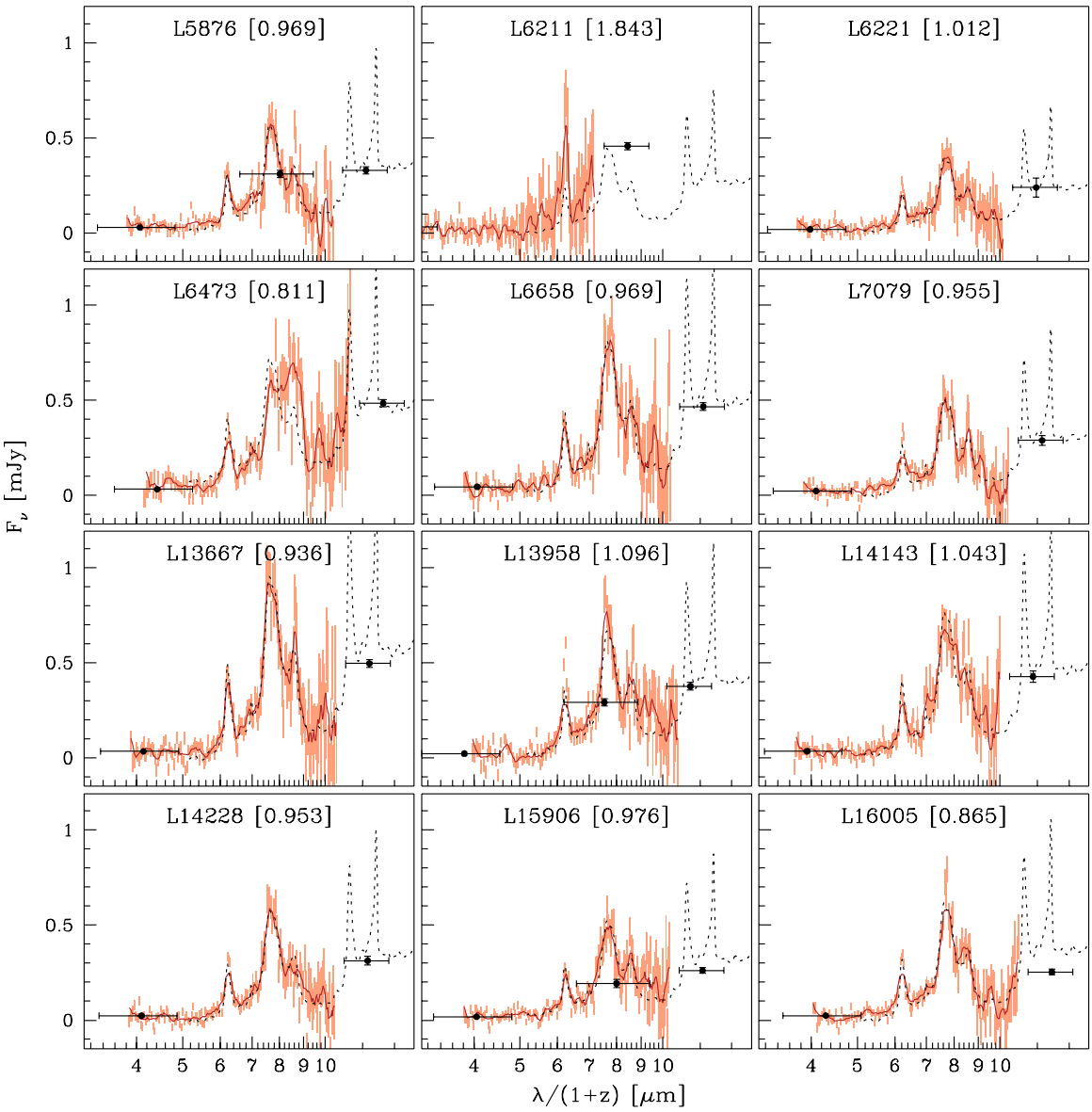

Figure 6. (Continued)

4.2. Mid-IR Spectroscopic Redshifts

Of our 48 sources, we were able to estimate redshifts for 44 of them from their mid-IR spectra based on the PAH emission features and silicate absorption. We estimated the redshifts by cross-correlating the averaged starburst template of Brandl et al. (2006). For three sources in the LIRG sample, we were not able to estimate spectroscopic redshifts from the IRS data because of the lack of recognizable features. When plotting their spectra with the broadband photometry points (see Figure 8), it is clear that two of them (L5511 and L6211) are at redshifts higher than those estimated by Caputi et al. (2006, 0.754 and 0.776, respectively). They are actually ULIRGs at $z = 2.08$ and 1.84, respectively. Furthermore, Figure 6 shows that the spectrum of L6211 has fairly strong 6.2 μm PAH emission at $z = 1.84$, with the rest of the PAH spectrum not sampled by the observations (LIRG observations used only LL1, not LL2). The wrong estimates are due to wrong identifications with optical sources at $\sim 1\farcs5$ from their positions. The real counterparts are faint sources very close to these bright galaxies and usually blended with them in ground images which are not reported in the COMBO17 catalog. The faint optical counterparts appear very clearly in the *HST* images (see Figure 24).

Figure 9 compares mid-IR spectroscopic redshifts with two sets of photometric redshifts in the top panel and with the optical spectroscopic redshifts in the bottom panel. The mid-IR spectroscopic redshifts are consistent with the available optical spectroscopic and photometric redshifts within 20%, and the photometric redshifts have larger uncertainties than those of mid-IR spectroscopic redshifts. The photometric redshifts from Wuyts et al. (2008) have a slightly lower dispersion than those from Caputi et al. (2004) since they are based on optical and infrared data. Table 3 reports preferentially photometric redshifts from the former study. We conclude that our sample selection based on initial photometric redshifts has proven effective.

Our IRS spectra have provided eight new spectroscopic redshifts used in Wuyts et al. (2009c) for which ground-based optical/near-IR spectroscopy is difficult. Particularly, at $z \sim 1.7$–2.0, Hα falls between the *H*- and *K*-band atmospheric

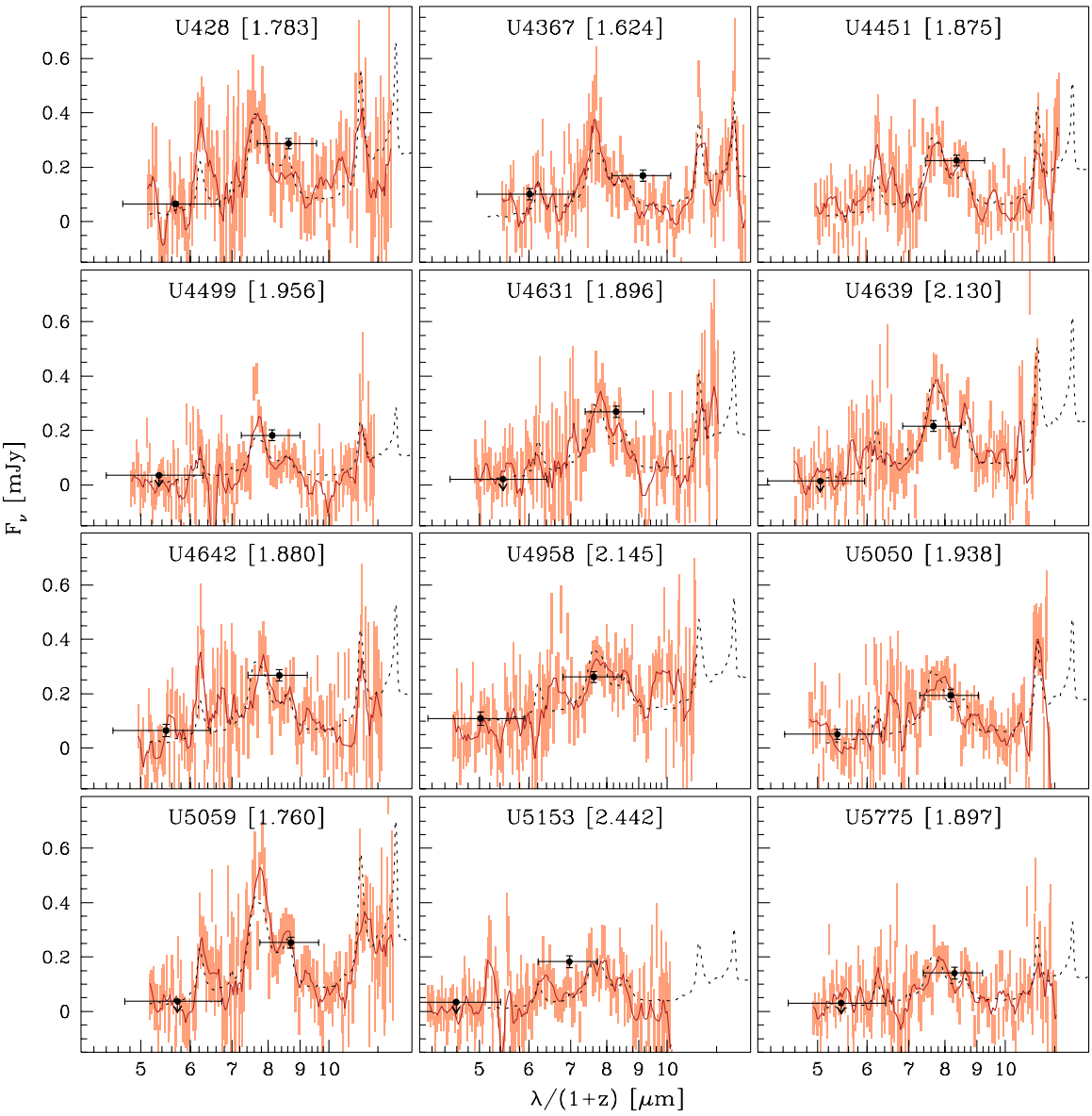

Figure 7. Observed spectra for our sample of 24 ULIRGs. The solid line, corresponding to the data with a smoothing of 5 pixels, is on the top of the shaded 1σ error bars for each pixel. broadband fluxes are overplotted. Dotted lines are either the averaged local starburst template from Brandl et al. (2006) or the hot dust dominated spectrum from Spoon et al. (2007) rescaled to the data. Source names and redshifts appear on the top of each panel.

(A color version of this figure is available in the online journal.)

windows, making ground-based near-IR spectroscopy impossible. For 24 μm galaxies in this redshift range, their *Spitzer* mid-IR spectra provide useful distance measurements.

4.3. AGN Fraction

One motivation for this program is to use mid-IR spectral diagnostics to determine the contribution of AGNs to the total energy output among LIRGs at $z \sim 1$ and ULIRGs at $z \sim 2$, particularly the obscured AGN which may not be detected by X-rays. It is important to understand that, although in some cases AGNs can completely dominate the bolometric luminosity, there is an entire population of galaxies with enshrouded AGNs whose bolometric luminosities are primarily from star formation. To objectively classify AGNs, we use several indicators such as: broad lines and high ionization lines in optical spectra, lack of a 1.6 μm stellar bump in the SED, X-ray bright sources, low mid-IR 6.2 μm PAH equivalent width (EW), and finally their optical morphology. We note that our samples at $z \sim 1$ and $z \sim 2$ now have 22 and 26 sources, respectively, because two galaxies initially assumed to be LIRGs at $z \sim 1$ have now been determined to be ULIRGs at $z \sim 2$ (see Section 4.2).

The 2 Ms *Chandra* X-ray survey covers all the ULIRGs and most of the LIRGs of our sample. Six of our sources have X-ray counterparts from the catalog of Luo et al. (2008, see Table 1). Two of them, U4950 and U5877, are clearly detected in the (2–8) keV hard X-ray band. Another one (U4642) is detected at the limit of sensitivity of the survey. Two more ULIRGs (U5775 and U428) are detected only in the soft X-ray and one LIRG (L5420) is detected at a low-σ level in the soft X-ray (secondary catalog). A cross-match with the more extended X-ray observations of Lehmer et al. (2005) does not yield any further counterpart. Figure 10 compiles all of the broadband photometry and mid-IR spectra for these six sources. U4950

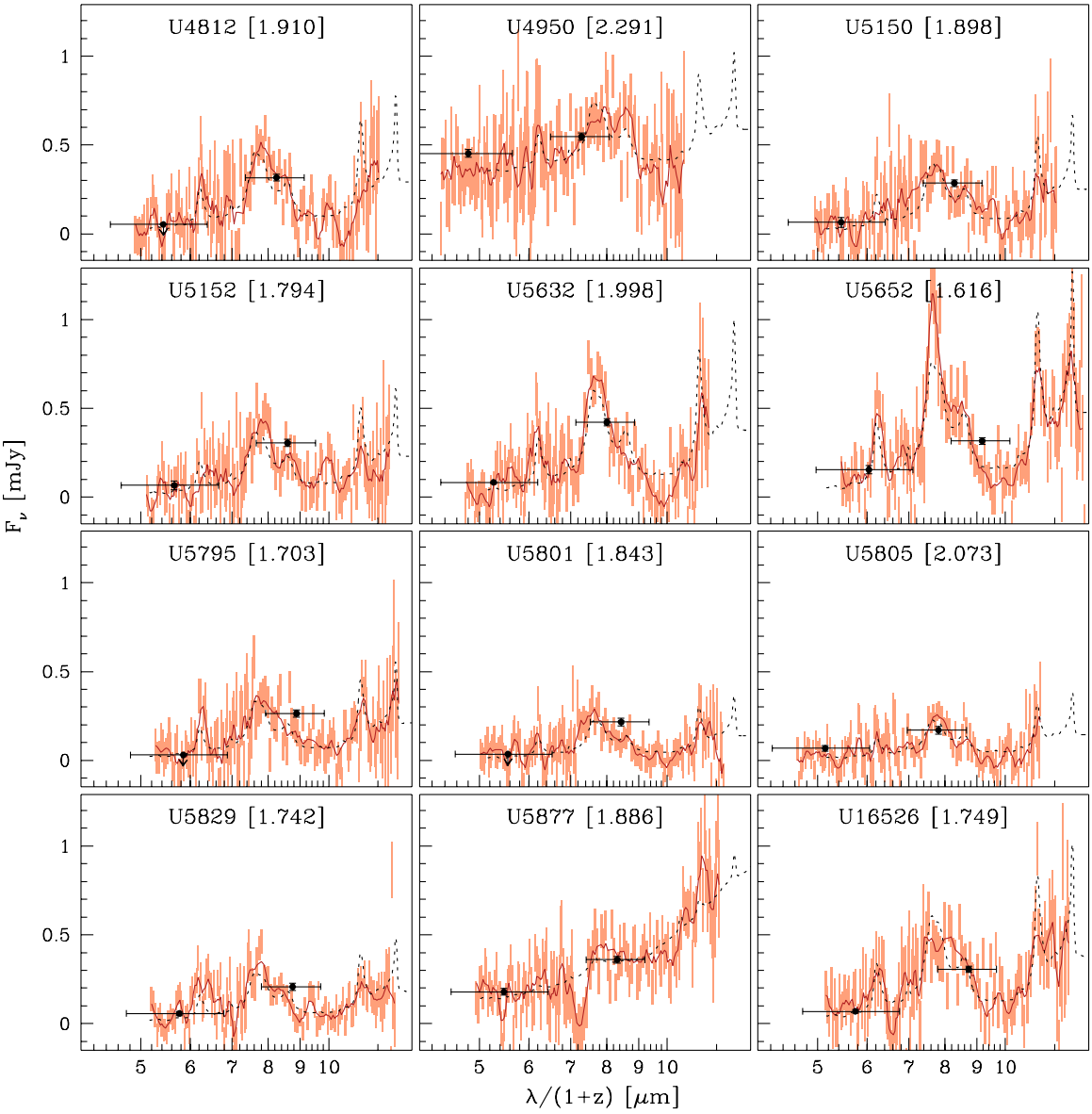

Figure 7. (Continued)

and U5877 have IRS spectra compatible with a power law and also their broadband photometry is typical of an AGN, i.e., no 1.6 μm stellar bump and a power-law spectrum over the entire wavelength range. We note that the *HST* morphologies of U4950 and U5877 show compact, unresolved nuclei, supporting the AGN classification from both X-ray and mid-IR spectra. The other source detected in the hard X-ray (U4642) has, on the contrary, a more complicated morphology with multiple clumps. So, one clump can host the AGN, but the AGN does not dominate the optical-IR emission. All the other sources (U5775, U428, and L5420) have a softer X-ray emission, the mid-IR spectra have obvious PAH emission (see the quantitative numbers below) and their broadband SEDs shown in Figure 10 reveal a strong stellar bump at rest-frame wavelength 1.6 μm, suggesting that although these three sources may have low-luminosity AGNs, their host galaxies dominate the stellar emission in optical to near-IR. The X-ray luminosity of the fainter X-ray sources is also compatible with star formation using the relationships from Ranalli et al. (2003).

The optical spectrum of U4958 (see Figure 5) shows a broad C III line and strong N V and C IV emission lines. Considering that the infrared spectrum is rather featureless, we can classify this source as AGN dominated.

The strength of PAH features has been widely used as a star formation indicator (Lutz et al. 1996; Genzel et al. 1998; Armus et al. 2007; Veilleux et al. 2009). Particularly, the 6.2 μm PAH is relatively isolated, and its rest-frame EW can be measured cleanly and used to classify starburst-dominated systems. This is supported by the fact that EW$_{6.2\,\mu m}$ is shown to broadly anti-correlate with flux ratios of [Ne V]/[Ne II] and [O V]/[Ne II] (Lutz et al. 1996; Genzel et al. 1998; Armus et al. 2006; Veilleux et al. 2009), where the detections of [Ne V]λ14.3 μm and [O IV]λ25.9 μm indicate the excitation of the ionized gas by black hole accretion due to their extremely high ionization potentials (97.1 eV and 59.4 eV respectively). We used the code PAHFIT (Smith et al. 2007) to fit lines and dust features together with a continuum from dust and stellar emission to our IRS spectra. During our analysis, we discovered two bugs in

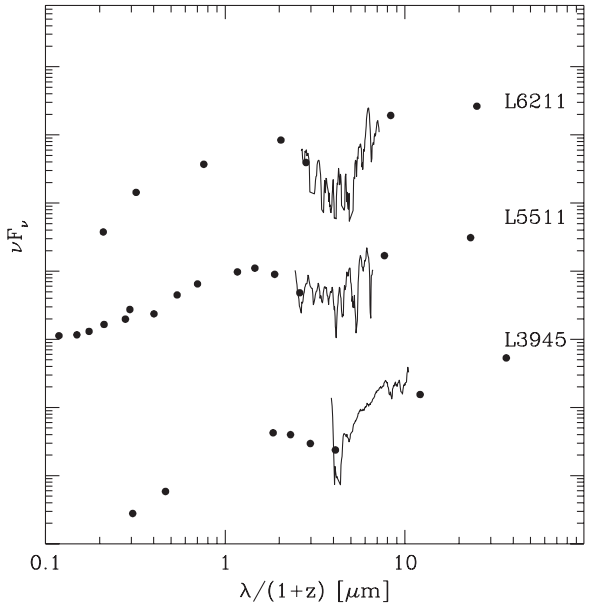

Figure 8. Available broadband fluxes and IRS spectra for three LIRGs without strong PAH features. The photometric redshifts used in the sample selection were 0.754 and 0.776 for L5511 and L6211, respectively (Caputi et al. 2006). The proposed redshifts of 2.08 and 1.84 for L5511 and L6211, respectively, correctly place the valley between the parts of the SED dominated by stellar and dust emission as well as a strong feature visible in the L6211 IRS spectrum (identified as 6.2 μm PAH).

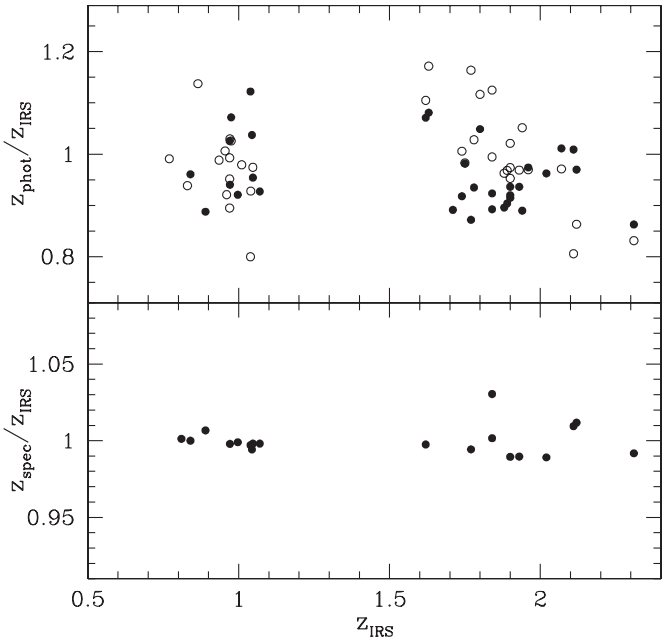

Figure 9. Comparison between mid-IR spectroscopic redshifts and optical redshifts (spectroscopic and photometric). In the top panel, photometric redshifts are from Wuyts et al. (2008, filled circles) and Caputi et al. (2006, open circles).

the routine that computes EWs. The routine was incorrectly applying Gaussian profiles instead of Drude profiles in the computation and, more importantly, using the flux of the line corrected for extinction and not corrected continuum. These bugs have been reported to the author of the code and will be fixed for the next release. To measure the EW of the 6.2 μm PAH, we used a Chiar–Tielens silicate profile and added an absorption component to take into account the water ice and hydrocarbon features at 5.7–7.8 μm. Following Veilleux et al. (2009), we used

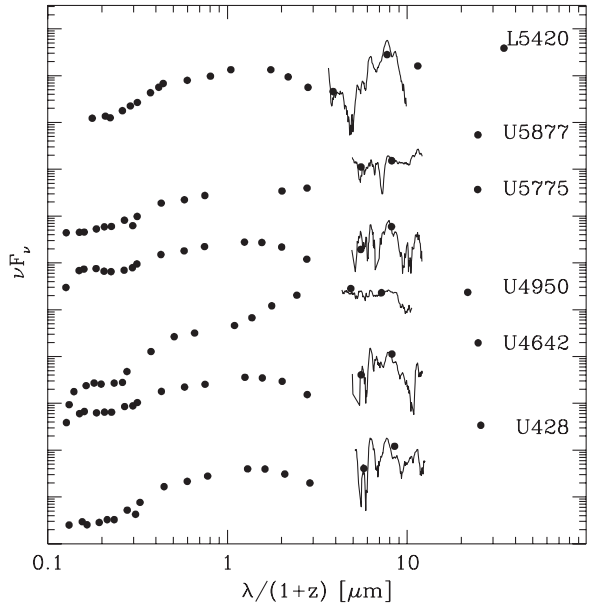

Figure 10. Broadband photometry and IRS spectra for the six IRS sources with X-ray counterparts. Only two of them (U4950 and U5877) have SED and spectral features compatible with AGN-dominated sources.

the profile taken from observations of F00183−7111 (Spoon et al. 2004) for this absorption feature. The addition of the water ice and hydrocarbon absorption features at 5.7–7.8 μm is important mainly in strongly absorbed local ULIRGs (see Section 4.6). Neglecting this component in our sample spectra and other high-z spectra does not significantly change the $EW_{6.2\,\mu m}$ estimates.

In the case of LIRGs, the signal-to-noise ratio of the spectra is high enough to measure directly the EW of the 6.2 μm PAH feature. In the case of ULIRGs, the low continuum combined with the higher noise of the spectra lead to large errors in the estimates of $EW_{6.2\,\mu m}$. In particular, the error is dominated by the uncertainty in the estimate of the continuum from the spectrum. To obtain firmer estimates for individual sources, we used 16 μm fluxes as estimates of the continuum since they have a much lower uncertainty. We have 16 μm fluxes for 14 ULIRGs and upper limits for an additional 9. Although, in general, most of the 16 μm flux is due to the continuum, the contribution of the 6.2 μm PAH is increasingly important at redshifts lower than 1.7. To compensate for this effect, we applied a multiplicative correction to the 16 μm flux equal to the ratio of the 5.8 μm flux and the expected 16 μm of the averaged starburst spectrum moved at the redshift of the ULIRG. This correction ranges from 0.6 at $z \sim 1.6$ to 0.9 at $z \sim 2$ and does not vary significantly by using different templates as the average HII-like ULIRG spectrum which better describes ULIRGs around the Si absorption. We were able to measure the $EW_{6.2\,\mu m}$ for all the sources with the exception of U4958 which we already classified as AGN on the basis of its optical spectrum.

The 6.2 μm EWs of the X-ray emitting sources are reported in Figure 11 and support our previous discussion. Studies of local LIRG and ULIRG spectra have shown that the percentage of AGN contribution to the total energy output correlates with $EW_{6.2\,\mu m}$. Armus et al. (2007) estimates that $EW_{6.2\,\mu m} < 0.3$ μm are AGN-dominated, where Veilleux et al. (2009) put the limit around 0.1 μm, while at 0.3 μm the AGN contribution is around 30%. The two results are not in contradiction since Veilleux

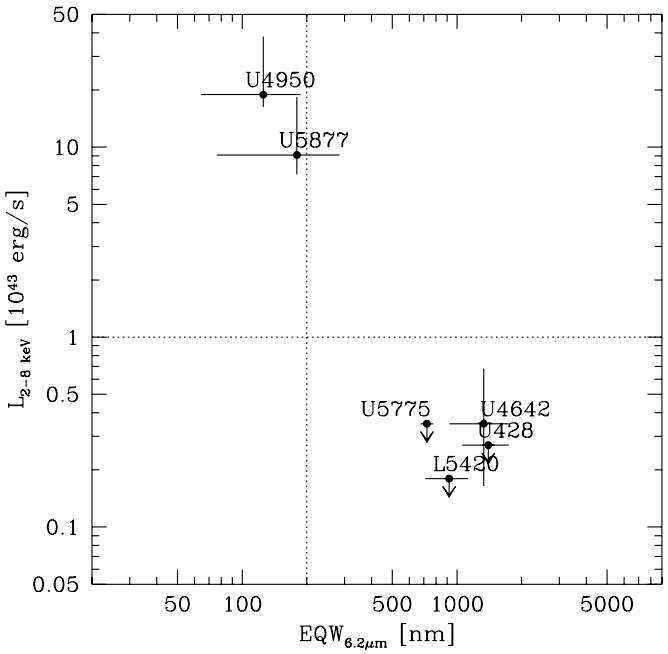

Figure 11. Hard X-ray 2–8 keV luminosity vs. EW of the 6.2 μm PAH feature for the IRS sources with X-ray counterparts. The infrared output of the objects on the left of the vertical line is dominated by AGN emission (Armus et al. 2007; Veilleux et al. 2009). Objects above the horizontal line are typically AGN-dominated sources (see, e.g., Fadda et al. (2002)). The dashed vertical line marks $EW_{6.2\,\mu m} = 0.2$ μm, below which galaxies are AGN dominated. See Section 4.3 for a detailed discussion of this value.

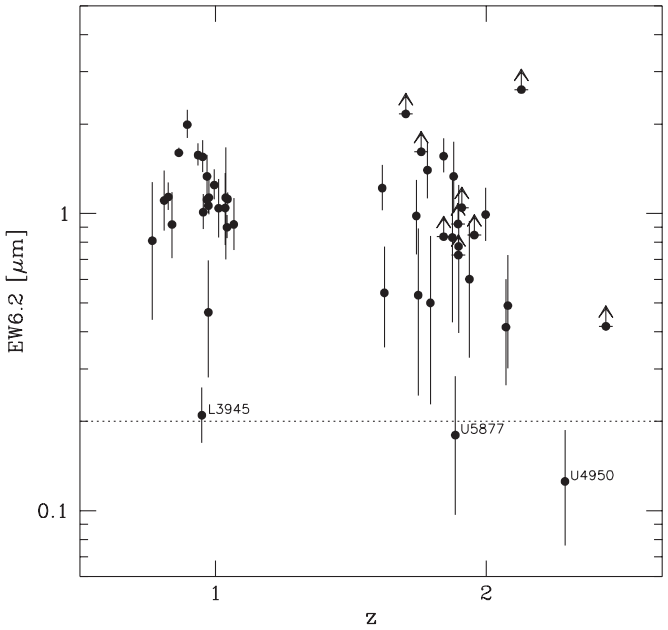

Figure 12. 6.2 μm EW vs. redshift. The lower limits come from upper limits to the continuum from 16 μm observations. The horizontal line corresponds to the limit between AGNs and star formation dominated systems. $EW_{6.2\,\mu m} = 0.2$ μm is derived from the combination of Armus et al. (2007) and Veilleux et al. (2009).

et al. (2009) compare AGN fractional contributions to the bolometric luminosities by applying bolometric corrections to their numbers (see Table 10 in Veilleux et al. 2009 and discussion in the Appendix). Armus et al. (2007) instead compare AGN fractional contributions to the [Ne II] and mid-IR luminosities. Nevertheless, according to other criteria used by Veilleux et al. (2009), sources with $EW_{6.2\,\mu m}$ up to 0.2 μm can also be AGN-dominated (see Figure 18). In the following, we assume 0.2 μm as a conservative limit.

Figure 11 shows that the mid-IR 6.2 μm PAH equivalent criteria have yielded the same conclusion as we stated above, that two X-ray sources U4950 and U5877 are strong AGNs, and the rest of the four have their infrared emission dominated by star formation.

Since many LIRGs are outside of the X-ray field or in the less sensitive parts and because of the limited hard X-ray sensitivity, it is useful to analyze the 6.2 μm EWs of our entire sample. Figure 12 shows the 6.2 μm EW versus redshift for all 48 sources with measurable 6.2 μm PAH. The infrared emission of almost all the LIRGs and the majority of the ULIRGs are dominated by star formation. The LIRG with low 6.2 μm EW (L3945) lie in the less sensitive and external regions of the X-ray survey and therefore it is not a surprise that it is not detected.

Among LIRGs, therefore only one source is dominated by the AGN emission (5% of the sample). In the case of ULIRGs, we exclude L5511 (reclassified as ULIRG) from the sample because its spectrum does not have enough coverage to yield usable 6.2 μm EW measurement. Thus, of the total 25 ULIRGs at $z \sim 2$, only 12% (3/25) have a dominant AGN.

These numbers are significantly lower than those for bright ($S_\nu \gtrsim 1$ mJy) 24 μm samples in the same redshift range. Based on the mid-IR spectral features as well as IR SEDs, the fraction of AGNs dominating the IR luminosities are close to (50–75)% (Yan et al. 2005, 2007; Sajina et al. 2007, 2008). Including weak AGNs or starburst/AGN composite systems, the majority ($\gtrsim$ 75%) of bright 24 μm samples contain AGNs (Sajina et al. 2008). Studies of local ULIRGs have found that the AGN fraction becomes significant at $L_{IR} \gtrsim 10^{12.3}\,L_\odot$ (Lutz et al. 1998), although the exact numbers suffer from many uncertainties. There are speculations (see Section 4.6) that at high-z, this AGN-starburst transitional luminosity moves to higher values. One piece of supporting evidence has been sub-millimeter galaxies (SMGs), whose L_{IR} is on average $\gtrsim 10^{12.3}\,L_\odot$, and it is commonly accepted that bolometric luminosities of SMGs are mostly from starbursts (see, e.g., Alexander et al. 2003; Valiante et al. 2007). One result from this paper is that the AGN fraction for $z \sim 2$ galaxies is small for $L_{IR} \sim 10^{12.6}\,L_\odot$, which implies that at high-z, the AGN-starburst transitional luminosity must be higher than $L_{IR} \sim 10^{12.6}\,L_\odot$.

4.4. Stacked Mid-IR Spectra

How do the relative PAH strength of high-z LIRGs and ULIRGs compare with those of local infrared galaxies? As shown in Figures 6 and 7, our individual spectra are very similar to the averaged $z \sim 0$ starburst spectrum (Brandl et al. 2006). We note that our spectra are typically not deep enough to individually probe the silicate absorption feature at 9.7 μm. In this section, we make this comparison by producing stacked spectra at z of 1 and 2 redshift bins. This technique has been widely used in recent years to detect and quantify certain weak features which are not detected in the data of individual sources.

We exclude from stacking the few sources whose emission is AGN-dominated: three ULIRGs (U4958, U4950, and U5877) and one LIRG (L3945), as explained in Section 4.3. We choose to normalize the spectra to their 24 μm rest-frame luminosity which correlates with their total infrared luminosity (Rieke et al. 2009). Here, the rest-frame 24 μm luminosity is calculated differently for the two samples. For $z \sim 1$ LIRGs, we simply interpolated the 8, 24, and 70 μm fluxes in the log(λ) versus

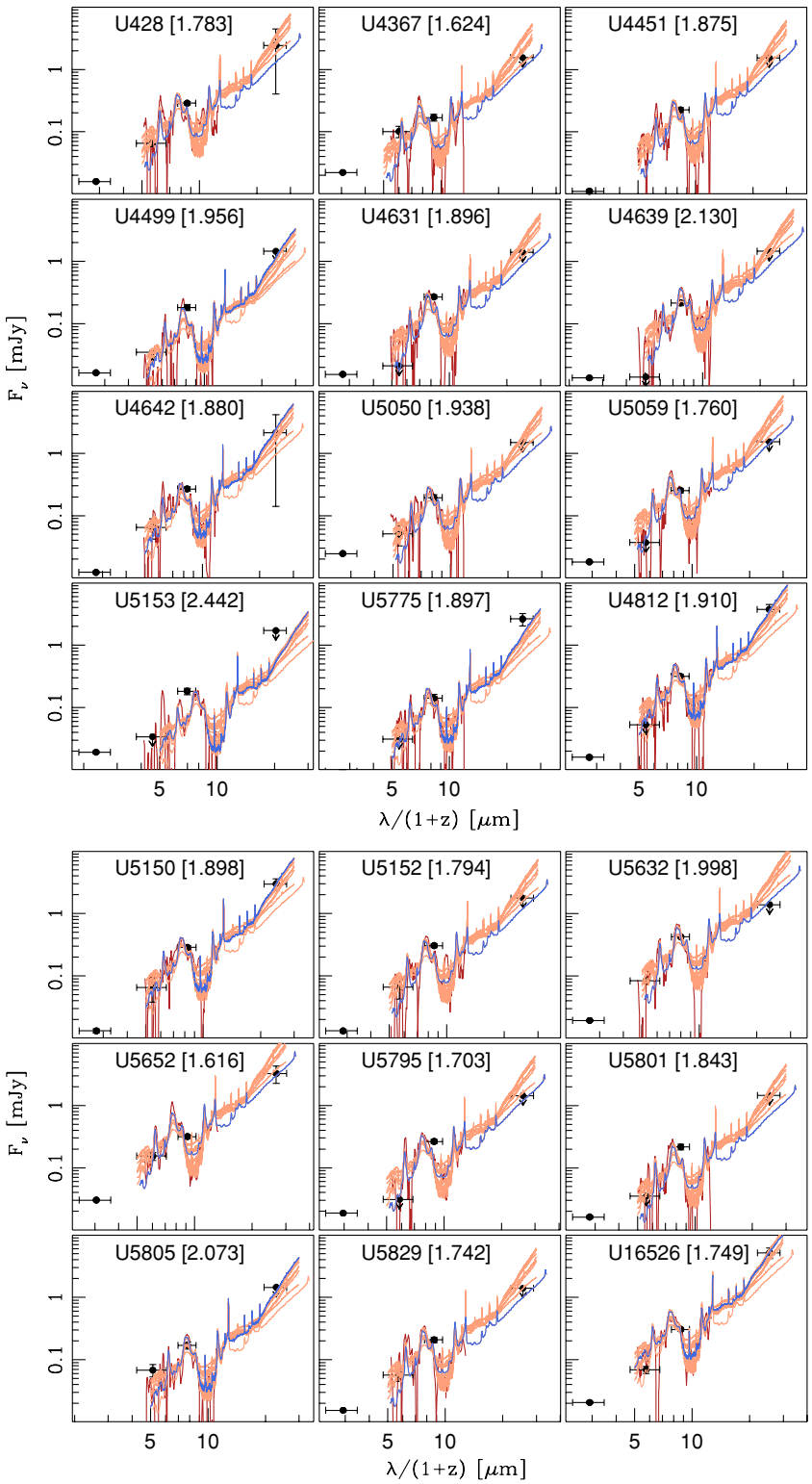

Figure 13. Templates of average starburst (Brandl et al. 2006) and ULIRG composites (Veilleux et al. 2009) rescaled to the smoothed IRS spectra (red line) of non-AGN-dominated ULIRGs. The best fit compatible with the 70 μm flux is shown in blue.

(A color version of this figure is available in the online journal.)

log(ν F_ν) plot. We do not consider the 16 μm flux since it is severely affected by the 7.7 μm PAH complex. In the case of $z \sim 2$ ULIRGs, the 70 μm flux is very close to the rest-frame 24 μm flux. Unfortunately, for many ULIRGs we have only upper limits of the 70 μm fluxes. In these cases, we estimate the rest-frame 24 μm fluxes by scaling a series of templates, including the averaged starburst from Brandl et al. (2006) and the composite ULIRGs from Veilleux et al. (2009), to fit the spectrum. The best-fitting template compatible with the 70 μm flux or upper limit is then considered to estimate the rest-frame 24 μm flux. The rescaled templates are shown in Figure 13. In Table 3, we list the estimated total infrared luminosities.

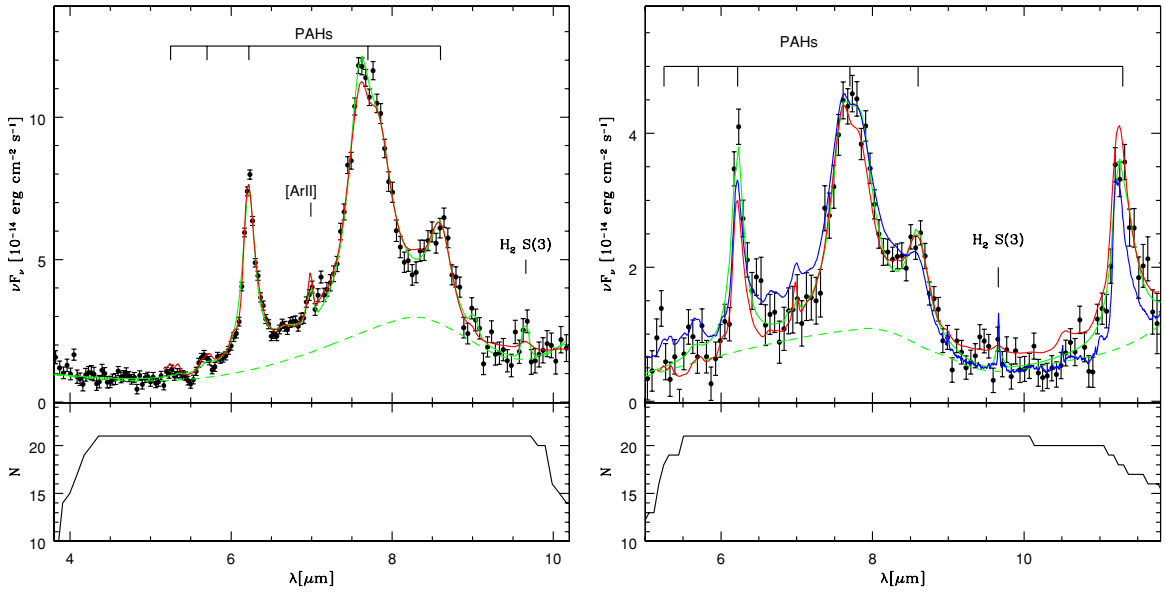

Figure 14. Averaged $z \sim 1$ LIRG (left) and $z \sim 2$ ULIRG spectrum (right) obtained by stacking all the spectra which are not AGN-dominated. The spectra have been normalized to the 24 μm rest-frame luminosity before stacking them. The lower panel shows the number of spectra used for each wavelength. The continued and dashed green lines correspond, respectively, to the total flux and continuum fitted with PAHFIT. The red and blue lines correspond, respectively, to the averaged starburst from Brandl et al. (2006) and the average local H II ULIRG from Veilleux et al. (2009) normalized to the stacked spectra.

(A color version of this figure is available in the online journal.)

The result of the stacking is shown in Figure 14. We have resampled the original spectra on a common wavelength grid as close as possible to the original data. At each wavelength, we computed the average values weighted by the errors on the single spectra. To check if outliers create artificial strong features, we also obtained spectra by using the biweight mean and we did find only negligible variations between the two methods.

The averaged spectra show clearly the characteristics of starburst-dominated galaxies with weak dust continuum at 4–14 μm and strong PAH emission at 6.2, 7.7, 8.6, and 11.3 μm. Weak PAH features at 5.25 and 5.70 μm are also visible, especially in the LIRG spectrum. For comparison, we also report in Figure 14 local average spectra normalized to our data (by minimizing the χ^2 of the residuals). The average LIRG is surprisingly close to the average starburst spectrum from Brandl et al. (2006). In the case of the average ULIRG, we compare it to the average starburst spectrum from Brandl et al. (2006) and to several average local ULIRG spectra from Veilleux et al. (2009). The best fit among the Veilleux et al. (2009) spectra is obtained using the H II-like ULIRG average spectrum. Although the average starburst spectrum fits well to the relative PAH strength in the averaged spectrum of $z \sim 2$ ULIRG, the local average ULIRG reproduces better the 9.7 μm silicate absorption. This implies that high-z ULIRGs have more dust extinction than lower luminosity LIRGs.

4.5. Comparison with Empirical IR SED Templates

Empirical IR SED templates used to model counts from deep surveys and the CIB are mostly based on local galaxies. One important question is how these empirical SEDs compare with our observed SEDs, including broadband photometry and spectra. Here, we considered all the spectra which are not dominated by AGN emission and obtained composite spectra by weighting the individual spectra by their total infrared luminosities. The same procedure has been applied to the IRAC and MIPS fluxes of the sources. The composite SED plus IRS spectra are compared to four different models, among the most popular, in Figures 15 and 16. For each model, we chose the one with closest total infrared luminosity and rescaled it to the total infrared luminosity of the composite spectrum. In the case of the Dale & Helou (2002) models, which give spectra as a function of the F_{60}/F_{100} color, we used the relationship between this color and the total infrared luminosity in Chapin et al. (2009).

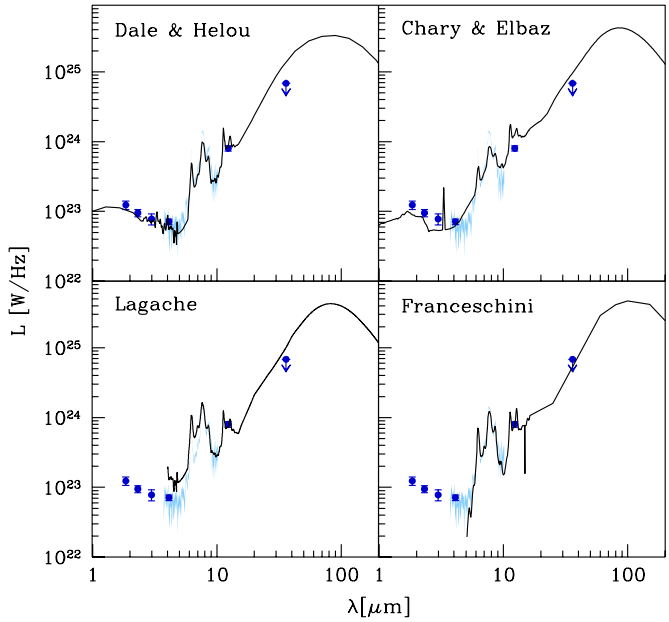

Figure 15. Composite LIRG spectrum and IRAC and MIPS fluxes compared to four popular theoretical templates (Franceschini et al. 2009; Lagache et al. 2004; Dale & Helou 2002; Chary & Elbaz 2001).

(A color version of this figure is available in the online journal.)

Two models extend down to near-IR fluxes (Dale & Helou 2002; Chary & Elbaz 2001), while the other two (Lagache et al. 2004; Franceschini et al. 2009) are limited to wavelengths longer than 4 μm. It is interesting to note that of the four empirical SED template models, only the Franceschini model templates fit the

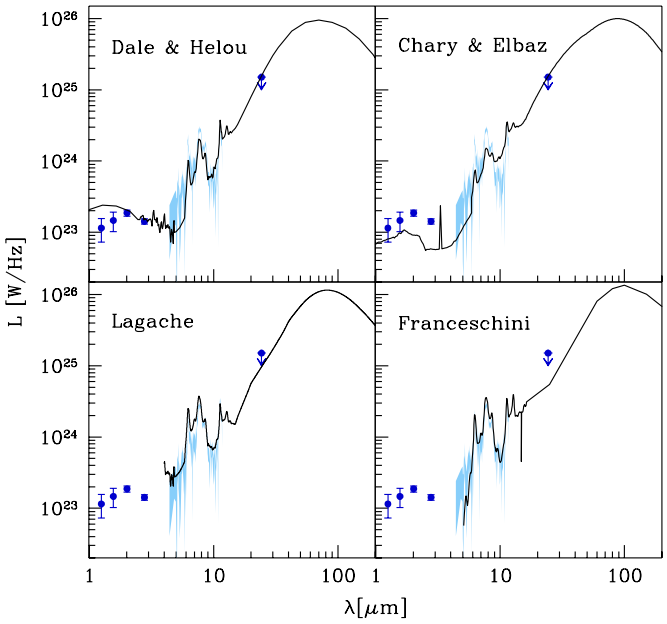

Figure 16. ULIRG spectrum and IRAC and MIPS fluxes compared to four popular theoretical templates (Franceschini et al. 2009; Lagache et al. 2004; Dale & Helou 2002; Chary & Elbaz 2001).

(A color version of this figure is available in the online journal.)

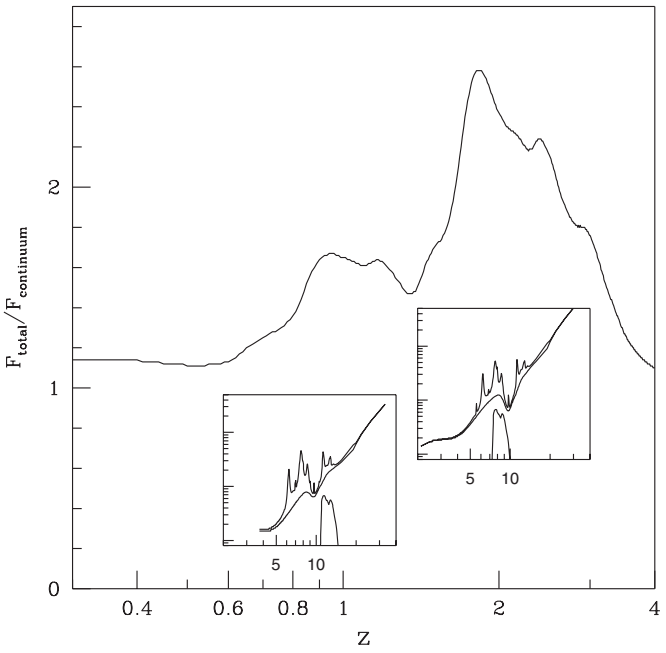

Figure 17. Fraction of the total over continuum 24 μm flux for luminous galaxies in the range between redshift 0 and 4, based on our composite LIRG and ULIRG spectra. The presence of PAH features boosts the detection of 24 μm sources around $z \sim 0.9$ and $z \sim 1.8$, the median redshifts of our two subsamples. The insets show the decomposition of the two composite spectra in PAH plus continuum and the locations of the 24 μm filter at the two sensitivity peaks.

mid-IR spectral features, although all four models are more or less in agreement with the overall observed SEDs for both LIRGs and ULIRGs. However, the few observational constraints in the far-IR part are consistent with all four templates. For LIRGs, only the Franceschini et al. (2009) model SED template agrees with the observed spectral features and is able to reproduce the far-IR limit for the observed LIRG composite.

Using the composite spectra plus the IRAC and MIPS fluxes, we also tried to estimate how much the presence of PAH features boosts the detection of infrared galaxies in the 24 μm filter as a function of redshift. As shown in Figure 17, we fitted the composite LIRG and ULIRG with PAHFIT to estimate the continuum. Then, we computed the ratio of the flux in the 24 μm filter for the total spectrum and for the continuum only. The ratio of these two fluxes has two clear peaks approximately at $z = 0.9$ and $z = 1.8$ which corresponds to the redshifts where the 24 μm filter includes the two main PAH complexes (11.3 and 7.7 μm). For comparison, the median redshifts of our two samples are 0.95 and 1.87. Figure 17 suggests that at $z \sim 2$, 24 μm broadband filter selection will preferentially select galaxies with strong PAH emission rather than power-law sources, and this bias can be as high as a factor of 2.

4.6. 6.2 μm Equivalent Width versus far-IR Luminosity

In this section, we explore the relationship between two quantities which are mainly linked to star formation: the rest-frame 24 μm monochromatic luminosity $(\nu L_\nu)_{24\,\mu m}$ and the EW of the 6.2 μm PAH feature. The rest-frame $(\nu L_\nu)_{24\,\mu m}$ is related to the total infrared luminosity $L_{IR} = L_{8-1000\,\mu m}$ (Rieke et al. 2009) which is an indicator of star formation. On the other hand, PAH features are created in star-forming regions and destroyed around AGNs, due to their intense ionization fields(see, e.g., Voit 1992; Lutz et al. 1998). We expect, therefore, that in presence of an AGN component, $(\nu L_\nu)_{24\,\mu m}$ is proportional to the sum of the AGN and starburst luminosities. On the other side, $EW_{6.2\,\mu m}$ is the ratio between the strength of the line (due only to star-formation activity) and the underlying continuum (created by AGNs and star-formation activity). These two quantities should behave like:

$$(\nu L_\nu)_{24\,\mu m} \propto (L_{AGN} + L_{SB}), \quad (1)$$

$$EW_{6.2\,\mu m} \propto \frac{L_{SB}}{L_{AGN} + L_{SB}}, \quad (2)$$

where L_{AGN} and L_{SB} are the AGN and starburst luminosities, respectively.

In Figure 18, we report the 6.2 μm EWs measured for the $z \sim 1$ LIRGs (blue dots) and ULIRG at $z \sim 2$ (black dots) as a function of their rest-frame 24 μm luminosities. We also plot the $EW_{6.2\,\mu m}$ of the composite ULIRG (black dot with error bar). The stacked ULIRG spectrum has a high enough signal-to-noise ratio to directly measure its mid-IR continuum and therefore obtain an average $EW_{6.2\,\mu m}$.

In Figure 18, we compare local starbursts (Brandl et al. 2006), 1 Jy ULIRGs (Veilleux et al. 2009) with a collection of high-z *Spitzer* ULIRGs and SMGs (Sajina et al. 2007; Menéndez-Delmestre et al. 2007; Pope et al. 2008; Valiante et al. 2009). We report also the average points from Desai et al. (2007) computed from local galaxies. To make this comparison meaningful, we re-measured $EW_{6.2\,\mu m}$ and $L_{24\,\mu m}$ for all of the sources included in Figure 18. We measured the $EW_{6.2\,\mu m}$ using our revised version of PAHFIT (see Section 4.3). The values of $EW_{6.2\,\mu m}$ for highly extincted ULIRGs agree very well with those computed by Veilleux et al. (2009). In contrast, for less extincted galaxies we have systematically lower values (~70%), probably due to the fact that Veilleux et al. (2009) do not directly fit the lines but uses templates to fit the spectra whose actual relative PAH strength may differ from that of the templates.

One striking result shown in Figure 18 is the maximum $EW_{6.2\,\mu m}$ value, ~ 1 μm, an upper limit for all starbursts, LIRGs and ULIRGs, independent of redshifts. This maximum limit is expected from Equation (1), indicating that when $L_{AGN} \ll L_{SB}$,

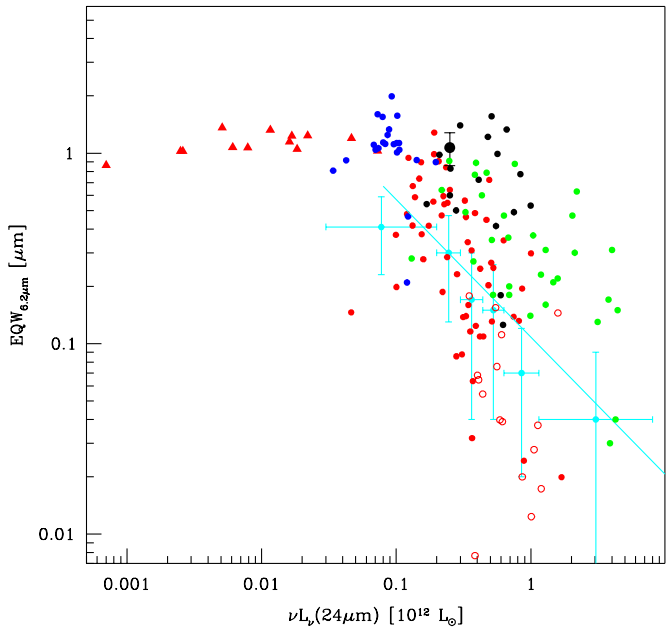

Figure 18. EW of the 6.2 μm PAH feature vs. the rest-frame luminosity at 24 μm for galaxies of our sample ($z \sim 1$ and $z \sim 2$ galaxies are marked with blue and black dots, respectively) compared to local and other high-z galaxies. We note that we re-measure $EW_{6.2\,\mu m}$ and $L_{24\,\mu m}$ for all objects in this figure. The black dot with error bars is for the average $z \sim 2$ ULIRG. The red triangles correspond to local starbursts from Brandl et al. (2006), while the red circles are ULIRGs from the local 1 Jy sample by Veilleux et al. (2009). The open circles are classified as at least 50% AGNs dominated by Veilleux et al. (2009). Finally, the green dots are high-redshift infrared sources from the literature (Sajina et al. 2007; Menéndez-Delmestre et al. 2007; Pope et al. 2008; Valiante et al. 2009). All the EWs have been remeasured in the same way as the one from our sample. Cyan points and line are from Desai et al. (2007).

$EW_{6.2\,\mu m}$ should be constant. We have no explanation why this constant is $\sim$1 μm. At $L_{24\,\mu m} \gtrsim 10^{11}\,L_{\odot}$, $EW_{6.2\,\mu m}$ and $L_{24\,\mu m}$ are clearly anti-correlated with a slightly different slope for local and high-redshift sources. The relation is broad not only because of errors in the measurement of the $EW_{6.2\,\mu m}$ but also due to AGN contributions that dilute the $EW_{6.2\,\mu m}$, intrinsically broadening the correlation. As a matter of fact, the dispersion of pure local starbursts (for which the AGN contamination is negligible) is much smaller than that of the local ULIRGs (which are contaminated by AGN).

Among high luminosity sources ($L_{24\,\mu m} > 10^{11}\,L_{\odot}$), at a given luminosity, high-redshift sources have PAH emission stronger than that of local ULIRGs. This can be interpreted in at least two different ways. Either high-redshift sources are forming stars more efficiently than local counterparts or local ULIRGs have a higher AGN contribution to their infrared continua. Supporting evidence for the first hypothesis is that SMGs at $z \sim 2$, which are the majority of the high-z luminous galaxies in our plot, have more gas, higher star formation rates, and more efficient star formation than local ULIRGs (Greve et al. 2005; Tacconi et al. 2006). On the other hand, if the AGN contribution to the mid-IR continuum is smaller for $z \gtrsim 1$ ULIRGs than that for local ULIRGs at a fixed luminosity, high-z ULIRGs would have bigger $EW_{6.2\,\mu m}$ due to less AGN boosting of the mid-IR continua. The good fit of the composed spectra of our sample with the averaged starburst template and the low estimated AGN contribution to their total emission (see also the next section) tend to support this last hypothesis.

4.7. Red Optical Colors

Many of our sources have very red optical SEDs. As shown in Figure 19, with definitions for ERG and distant red galaxies (DRG) of $(i - K)_{Vega} \gtrsim 4.0$ and $(J - K)_{Vega} \gtrsim 2.3$, respectively (Yan et al. 2000, 2005; Franx et al. 2003; van Dokkum et al. 2004), we find that of the 24 $z \sim 2$ ULIRGs, 63% (15/24) are ERGs and 33% (8/24) are DRGs. These near-IR color selected DRGs have very faint optical magnitudes, and their redshifts are difficult to obtain with optical/near-IR spectroscopy (Kriek et al. 2008). Our IRS spectra have provided eight spectroscopic redshifts which do not have optical spec-z and have been used

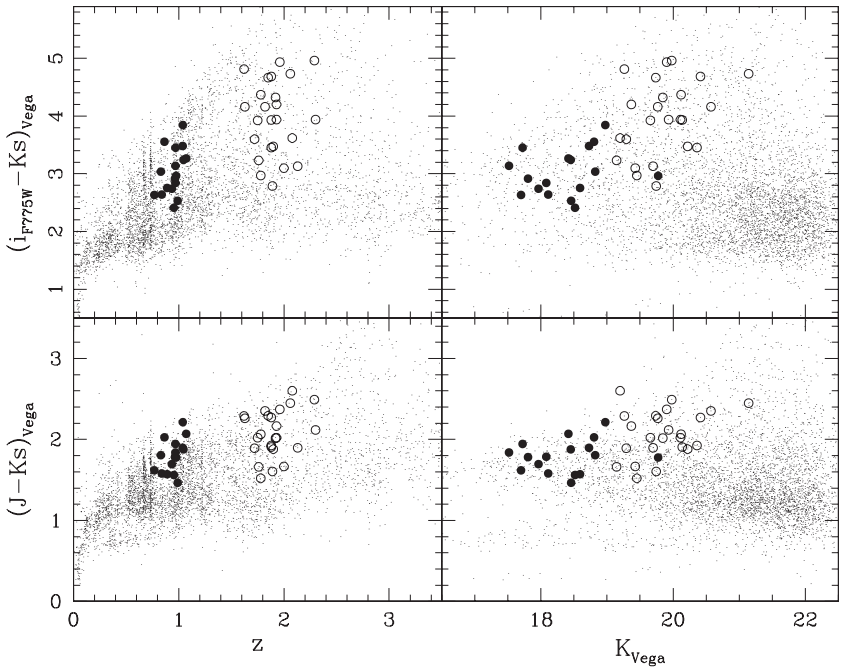

Figure 19. Color–color plots for galaxies in the GOODS field (dots) and galaxies of our sample. Filled and open circles mark the LIRGs and ULIRGs of our sample, respectively.

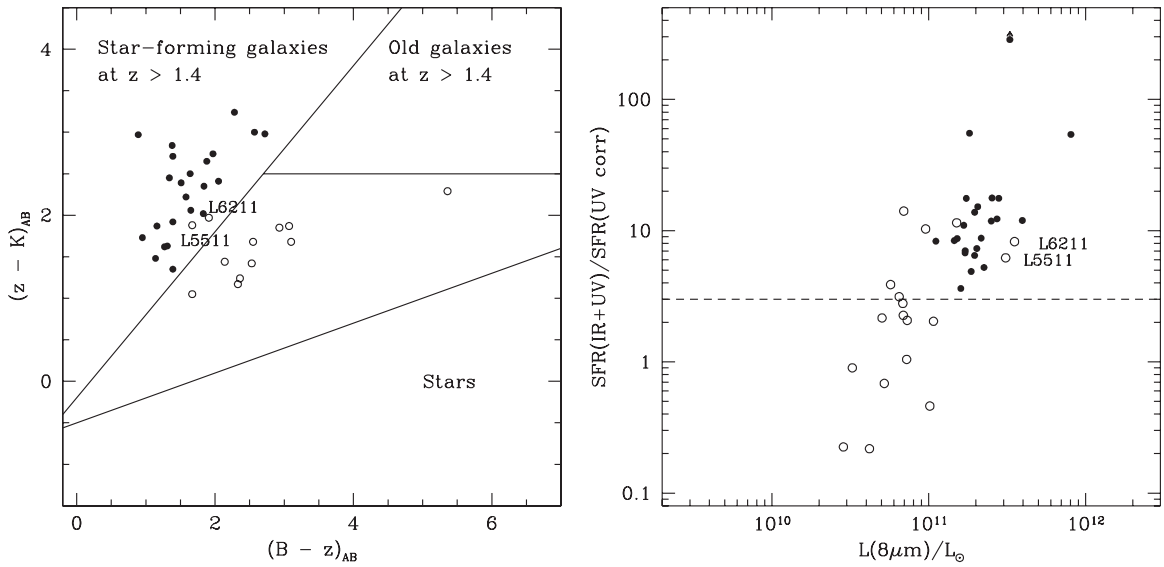

Figure 20. Left: optical/near-IR color plot; right: IR excess vs. rest-frame 8 μm luminosity. In the two figures, sources from the ULIRG and LIRG samples are marked with filled and open circles, respectively. The names indicate the two sources from the LIRG sample which are actually at redshift ~ 2.

for the analysis of the reliability of DRG color selections (Wuyts et al. 2009c). Our finding of eight $z \sim$2 ULIRGs having very red $(J - K)$ colors suggests that a significant fraction of DRGs selected by K-band surveys are dusty star-forming galaxies, not passively evolving stellar populations at $z \sim$ 2–3. This is consistent with previously published studies, which found as many as 50% of color-selected DRGs being dusty starbursts (Wuyts et al. 2007, 2009c; Labbé et al. 2005; Kriek et al. 2008).

Furthermore, all of the $z \sim 2$ ULIRGs also satisfy the $(z - B)$ versus $(K - z)$ color–color selections (BzK; Daddi et al. 2004), as shown in Figure 20. These BzK color cuts shown as lines in Figure 20 have been used to select star-forming and passively evolved galaxies at $z \gtrsim 1.4$ (Daddi et al. 2004). These $z \sim 2$ ULIRGs fall into the star-forming BzK region on the $(z-B)$ versus $(K-z)$ color–color diagram. As expected, their red BzK colors are mostly due to the dust absorption of the UV photons from O, B types of young stars produced by recent starbursts.

In Figure 20, we also report the IR excess as a function of $L_{8\,\mu\mathrm{m}}$ computed as in Daddi et al. (2004). All our $z \sim 2$ ULIRGs and a few LIRGs are IR excess galaxies according to the definition of Daddi et al. (2004). Although it is a known fact that optical and IR surveys select galaxies with different amounts of dust, the question here is if our IR selected galaxies follow the same dust extinction scaling relationship as optically selected objects with low dust content. Figure 21 shows the far-infrared to 1600 Å monochromatic luminosity ratio as a function of UV spectral index β, where $f_\lambda \sim \lambda^\beta$, 1000 Å $< \lambda <$ 2500 Å. The ratio $L_{\mathrm{FIR}}/L_{1600\,\text{Å}}$ measures how much energy is re-distributed from UV to infrared, and β measures the UV SED slope, i.e., UV reddening. Studies of local UV selected starbursts have shown that dust absorption is correlated with UV reddening (Meurer et al. 1995, 1999). This correlation provides a powerful empirical tool, particularly for high-z UV/optical surveys, to recover the total, dust-absorption corrected, UV fluxes, using UV photometry alone. Figure 21 compares the location of our sample with those of local galaxies (Meurer et al. 1999) and high-redshift galaxies (Chapman et al. 2005; Reddy et al. 2006) in the plot $L_{\mathrm{FIR}}/L_{1600\,\text{Å}}$ versus β. In the case of our sample, we used the available optical magnitudes from U to R to compute $L_{1600\,\text{Å}}$ by interpolating in νF_ν, while β was computed using the relationships from Papovich et al. (2006). The L_{FIR} is computed

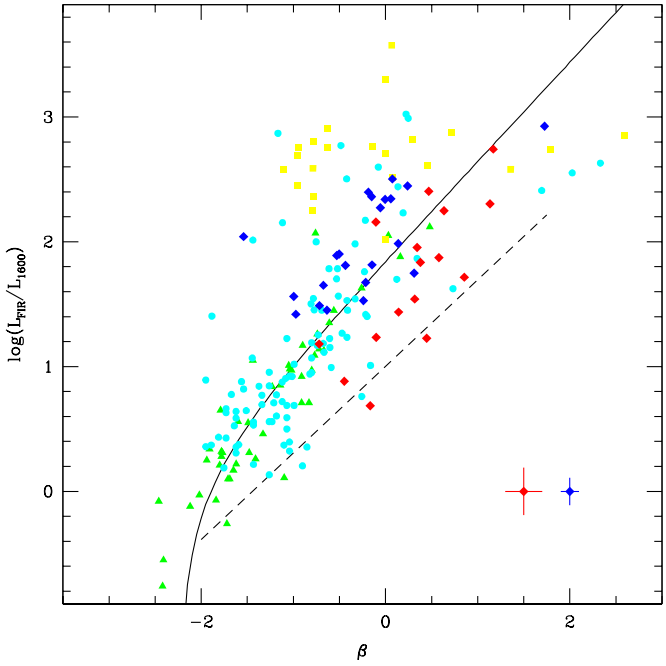

Figure 21. Ratio of far-IR to UV flux at 1600 Å compared to the UV spectral slope β for our galaxies and some published comparison galaxies. The solid line shows the linear fit to the $A_{1600\,\text{Å}}$–β relationship by Meurer et al. (1999). The dashed line shows the relation for normal star-forming galaxies (Cortese et al. 2006). The samples from Meurer et al. (1999), Reddy et al. (2006), and Chapman et al. (2005) are marked with green triangles, cyan dots, and yellow squares, respectively. Our $z \sim 1$ and $z \sim 2$ sample are marked with red and blue diamonds, respectively. The typical error of the points is shown in the bottom right corner of the plot. Most of our $z \sim 2$ ULIRG lie above the curve, in the region occupied by SMGs and HLIRGs.

(A color version of this figure is available in the online journal.)

from the rest-frame 24 μm luminosity using the relationship from Rieke et al. (2009) to compute the total IR luminosity and from Elbaz et al. (2002) to pass from total IR luminosity to far-IR luminosity. In the case of SMG galaxies from Chapman et al. (2005), we used the available B and R magnitudes to compute β and $L_{1600\,\text{Å}}$. The relationship from Papovich et al. (2006) was used after applying median corrections to the B and R

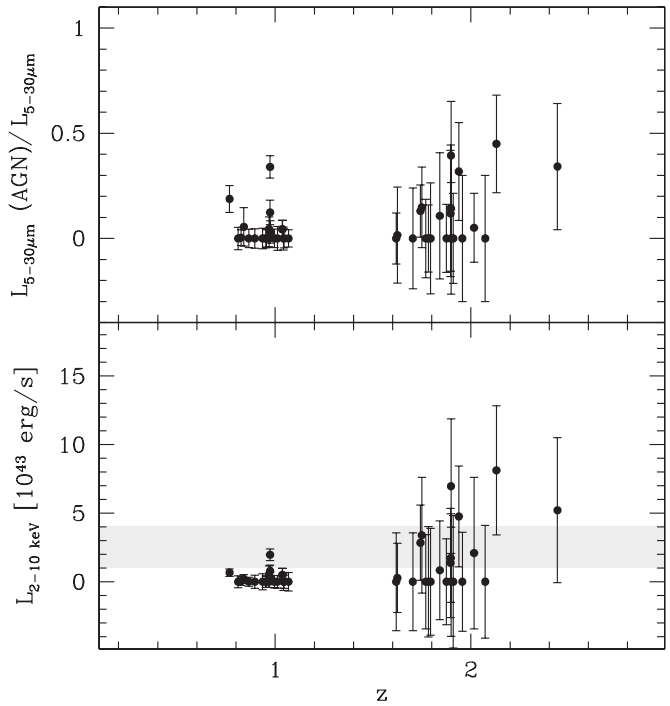

Figure 22. Fraction of the mid-infrared emission due to the AGN component and its X-ray luminosity (top and bottom panels, respectively) for the LIRGs and ULIRGs of our sample which are not dominated by AGN emission. The gray band marks the expected X-ray luminosity of obscured AGN according to Daddi et al. (2007).

magnitudes to transform them in the appropriate bands. For the $z \sim 1$ sample, the UV luminosity and β are poorly constrained since we do not have UV observations. These sources appear to scatter between the normal star-forming galaxies and the UV-selected starburst relations, which as discussed above can be attributed to a range of UV extinction slopes. For our $z \sim 2$ ULIRGs, we note that they largely lie above the Meurer's relationship, although usually not quite so far as the SMGs and HLIRGs (hyper-luminous IR galaxies). Overall, the large scatter in this diagram, and the strong dependence on the UV slope of the unknown extinction curve serve as caveats in applying standard UV dust corrections. Boquien et al. (2009) caution that applying the wrong extinction law to the UV would result in over- or underestimating the true SFR by factors of up to ~ 7. We return to this point in the following section.

4.8. "IR Excess" and Obscured AGN Luminosity

As discussed in Section 4.7, the BzK method has been used to study 24 μm galaxies in the GOODS field (Daddi et al. 2007). This paper found that as much as (20–30)% of $1.4 < z < 2.5$ BzK selected galaxies with $K_{\rm Vega} \lesssim 22$ have infrared excess, in the sense that $\rm SFR_{IR} + SFR_{UV,uncorrected} \gtrsim 3.16 \times SFR_{UV,corrected}$. Using the X-ray stacking method on these 24 μm galaxies with "IR excess," this study found that these galaxies contain highly obscured, Compton thick AGNs, and the predicted unobscured X-ray luminosity $L_{2-8\,\rm keV} \sim (1\text{–}4) \times 10^{43}$ erg s^{-1}. All our $z \sim 2$ ULIRGs are BzK galaxies satisfying the IR excess criteria (see Figure 20).

In principle, if we know the correct relationship to estimate $L_{\rm IR}$ from rest-frame $L_{8\,\mu\rm m}$, the correct UV extinction, and if the AGN contribution is negligible, we should get $\rm SFR_{UV,corrected} = SFR_{IR} + SFR_{UV,uncorrected}$. The fact that all our $z \sim 2$ ULIRGs have "IR excess" could be due to either (1) non-negligible AGNs contributing to total luminosities, or (2) wrong UV extinction correction, or (3) incorrect estimate of $L_{\rm IR}$. Daddi et al. (2007) have argued that this "IR excess" is primarily due to Compton-thick AGN heating of mid-IR luminosities, causing the overestimation of $L_{\rm IR}$, thus "excess" of $\rm SFR_{IR} + SFR_{UV,uncorrected}$. Our mid-IR spectra suggest that most $z \sim 2$ ULIRGs (92%) have strong PAH emission and AGN contribution to their $L_{\rm IR}$ is small. However, the rest-frame $L_{8\,\mu\rm m}$ estimated from observed broadband 24 μm photometry will be overestimated because of broad, strong PAH emission among starbursts. As already noted by Murphy et al. (2009), the relationship used by Daddi et al. (2007) to compute $L_{\rm IR}$ from $L_{8\,\mu\rm m}$ overestimates $L_{\rm IR}$. For our ULIRGs, the median ratio between SFR estimated from $L_{8\,\mu\rm m}$ and $L_{24\,\mu\rm m}$ is 3.1. Finally, another big factor causing this "IR excess" is the underestimated UV dust extinction correction. This is further supported by Figure 21, where the $z \sim 2$ ULIRGs are systematically offset above the local relationship defined by low luminosity, low extinction star-forming galaxies. It is not surprising that UV dust extinction of heavily obscured ULIRGs is only a lower limit because, for a mixed distribution of stars and dust, increasing amounts of dust will further absorb stellar emission, but the reddening of the integrated colors of a galaxy will saturate as the most obscured spectral regions have less weight in the integrated SED (Wuyts et al. 2009a).

Our IRS spectra illustrate that the "IR excess" feature in BzK galaxies is really due to strong broad PAH emission, particularly 7.7 μm feature, produced by recent starbursts. This excess is not due to dust being heated by obscured, Compton thick AGNs as stated in Daddi et al. (2007). Below, we will use the IRS spectra to qualitatively estimate obscured AGN luminosities.

Many mid-IR spectroscopic studies have shown that galaxies with obscured AGNs tend to have excess mid-IR continuum at 4–6 μm, which is thought to be produced by small, hot dust grains heated by UV photons from AGNs (Laurent et al. 2000). There is a narrow correlation between the AGN luminosity at 5.8 μm, $L_{5.8\,\mu\rm m}$, and its intrinsic X-ray luminosity $L_{2-10\,\rm keV}$ for local samples of Seyferts and QSOs:

$$\log L_{5.8\,\mu\rm m} = 1.209\ \log L_{2-10\,\rm keV} - 8.667 \qquad (3)$$

with luminosities expressed in erg s^{-1} (Lutz et al. 2004; Bauer et al. 2010).

To estimate the continuum due to the AGN emission at 5.8 μm, we fit to each spectrum a combination of a linear component plus the scaled average starburst template from Brandl et al. (2006) considering for the fit the 5.5–6.85 μm interval. This direct approach provides results consistent to the approach of Lutz et al. (2004) and Valiante et al. (2009) who used M82 as starburst template and adjusted for differences between M82 and an average starburst galaxy. To compare our results to the work of Daddi et al. (2007), we follow his criteria excluding galaxies detected in the 2–8 keV band in the 1 Ms *Chandra* survey and those without a clear decreasing in their SED after 1.6 μm. Therefore, we do not consider the two ULIRGs whose mid-IR spectra show very little PAH emission, have a power-law SED, and are clearly dominated by nuclear emission. We also exclude U4958 since its optical spectrum shows the presence of an AGN and the mid-IR spectra is almost featureless. Since several of the LIRGs of our sample are also "IR excess" galaxies, we apply the same analysis to this sample excluding three objects (L3945, L5511, L6211) which are not in the correct redshift range or have little or no PAH emission in their spectra.

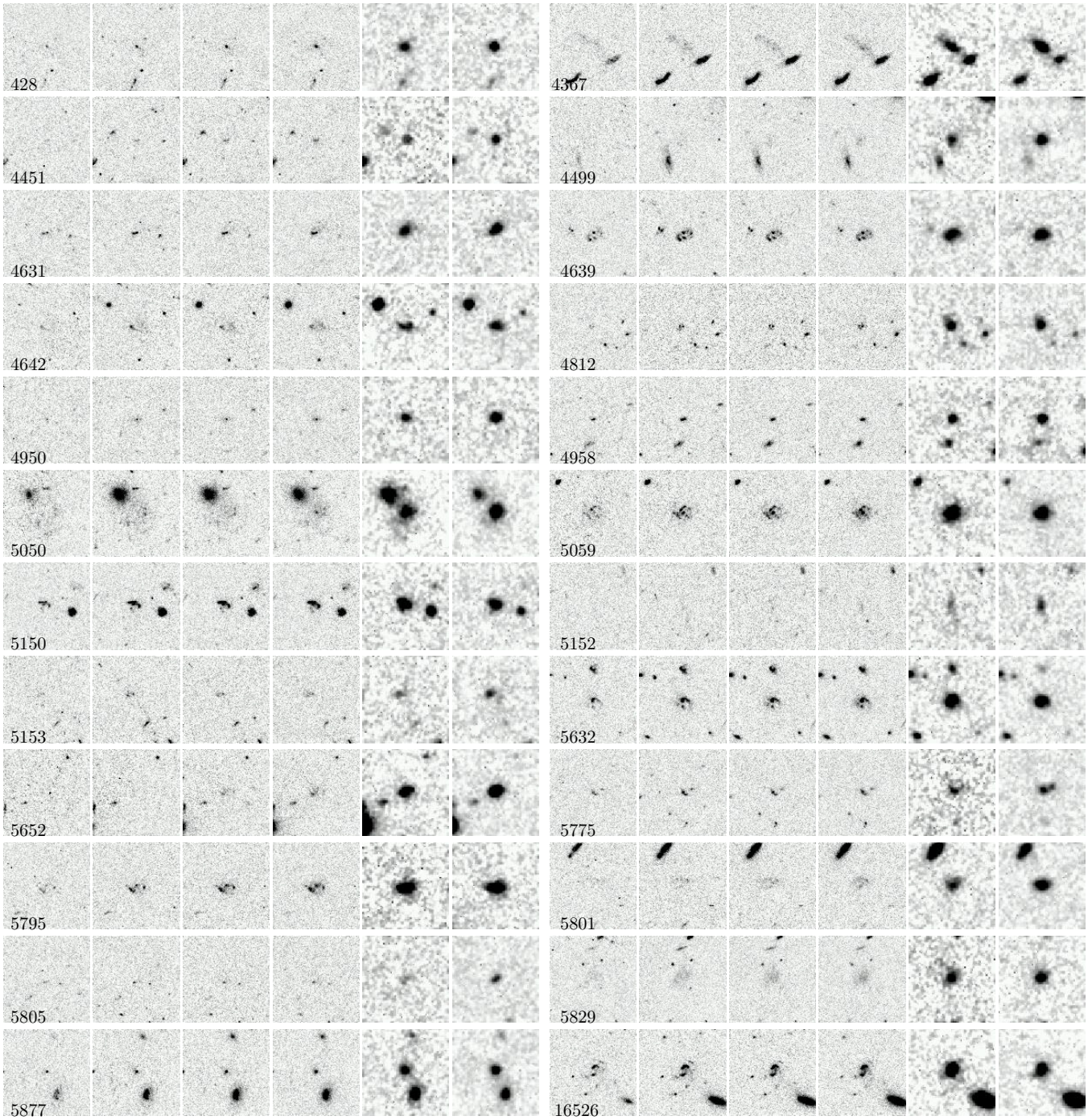

Figure 23. Image cutouts for each ULIRG are in the filters *F435W*, *F606W*, *F775W*, *F850LP* from *HST* ACS images of the GOODS treasury survey. *J* and *Ks* images are from the public EIS survey done with ISAAC on the VLT telescopes. The object ID is labeled on the *F435W* image. Each image stamp is $10'' \times 10''$.

To estimate the AGN contribution to the total mid-IR emission, we proceed as Murphy et al. (2009) by scaling the SED of Mrk231 to the 5.8 μm AGN continuum and fitting the residual SED with the average starburst from Brandl et al. (2006). As shown in Figure 22, the emission from most of the ULIRGs and almost all LIRGs is completely dominated by star formation. This confirms and extends the analysis of Murphy et al. (2009), since our study is done on a bigger, fainter, and more homogeneous sample. Moreover, our analysis allows us to directly estimate the X-ray luminosity of the AGN harbored in the galaxies of our sample. In the bottom panel of Figure 22, we report the estimated X-ray luminosities of the AGN component of the LIRGs and ULIRGs of our sample compared to the predictions based on stacked X-ray analysis from Daddi et al. (2007). Also in this case, the majority of ULIRGs have AGNs with X-ray luminosities lower than these values. A straight average of the values found would give a value of $L_{2-10\,\mathrm{keV}} = (1.8 \pm 0.6) \times 10^{43}$ erg s^{-1} which would be compatible with the analysis of Daddi et al. (2007). A robust average, using a biweight estimator, gives a value of $L_{2-10\,\mathrm{keV}} = (0.1 \pm 0.6) \times 10^{43}$ erg s^{-1}. This means that a few galaxies with bright hidden AGN dominate the stacking of the faint infrared sources in the aforementioned analysis, highlighting the intrinsic danger of any stacking analysis. We can conclude that the infrared emission from the majority of our

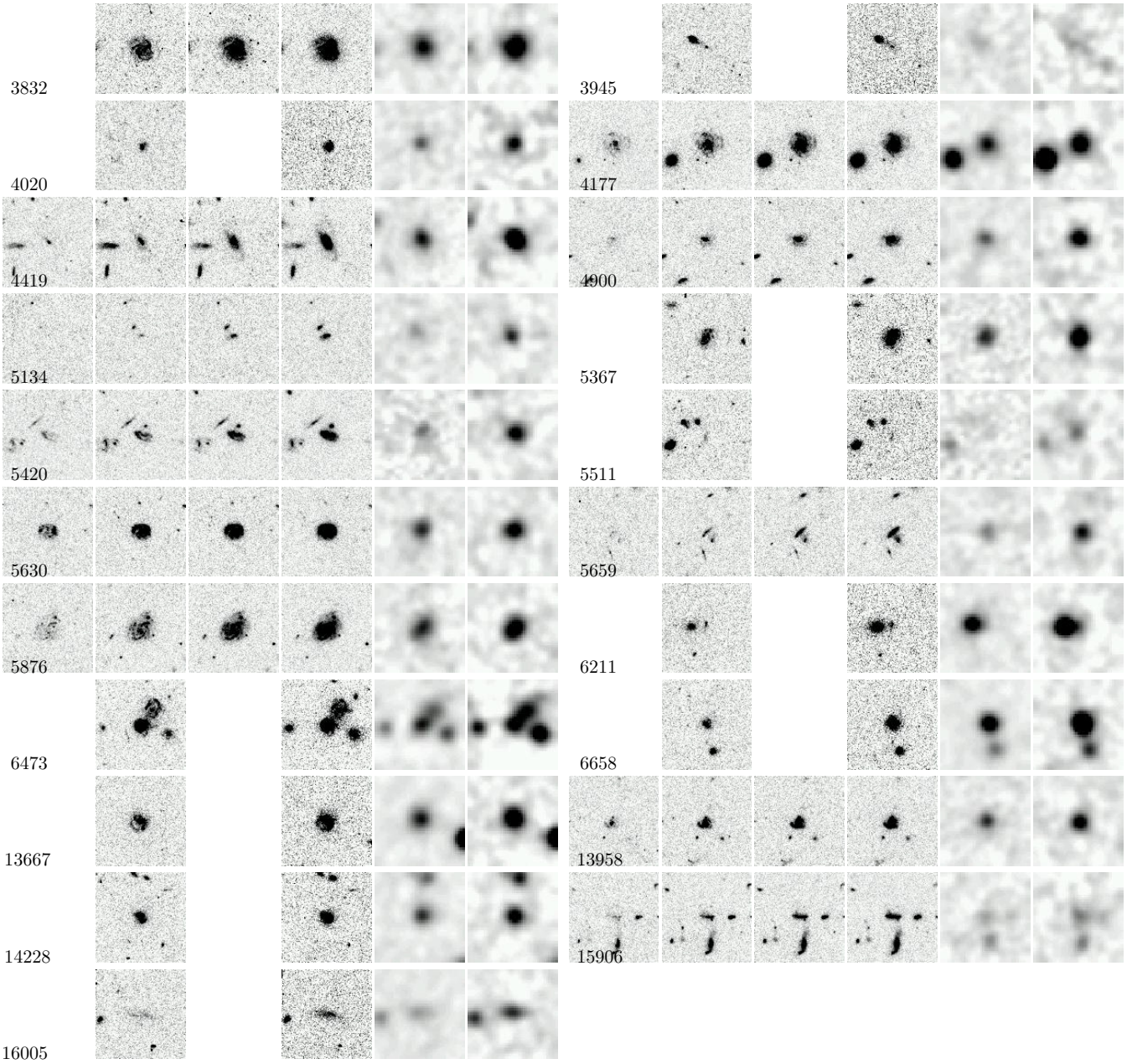

Figure 24. Similar to Figure 23, this plot shows the image cutouts for 21 LIRGs at $z \sim 1$. We used all of the available observations in *HST*/ACS *F606W* and *F850LP* filters for LIRGs within the GEMS survey, and *F435W*, *F606W*, *F775W*, and *F850LP* for LIRGs within the GOODS region. For objects in the GOODS region, *J* and *Ks* images are from the EIS survey. Otherwise, they are from the MUSYC survey (Gawiser et al. 2006).

ULIRGs (21/24, i.e., 88% of our sample) is dominated by star formation and the analysis of our sample of ULIRGs sets a low upper limit to the presence of Compton thick AGNs in LIRGs at $z \sim 2$, with respect to the analysis of Daddi et al. (2007).

In the case of LIRGs, the straight and robust average are $(0.2 \pm 0.1) \times 10^{43}$ erg s^{-1} and $(0.0 \pm 0.1) \times 10^{43}$ erg s^{-1}, respectively. We conclude that for the $z \sim 1$ sample, the majority of the galaxies do not harbor hidden AGNs and their emission is dominated by star formation.

4.9. Morphologies

LIRGs and ULIRGs shine at infrared luminosities of 10^{44}–10^{46} erg s^{-1}. It is not yet clear what physical processes light up a galaxy in the infrared and if major mergers are the dominant mechanism at $z \sim 1$–2, as is the case for local ULIRGs (Sanders & Mirabel 1996; Veilleux et al. 2002). The simplest way to address this question is to examine the morphologies of our sources using the high spatial resolution images from *HST*.

Figures 23 and 24 show image cutouts for ULIRGs and LIRGs, respectively, in the *HST F435W* (*B*), *F606W* (*V*), *F775W* (*i*), *F850LP* (*z*) bands and the ground-based *J* and *K* images. Each cutout has a size of $10'' \times 10''$. These two figures illustrate the steep changes of the spectral energy distribution from *B*–*K*, and clearly indicate that many of our sources have extremely red optical-to-NIR colors. To better show colors and morphologies, we present three-color images of the galaxies which have been observed with ACS in the *F435W*, *F606W*, and *F850LP* bands. The angular size of the images is $3''$ and $4''$ for ULIRGs and LIRGs, respectively, which corresponds to 25.2 kpc and 31.2 kpc

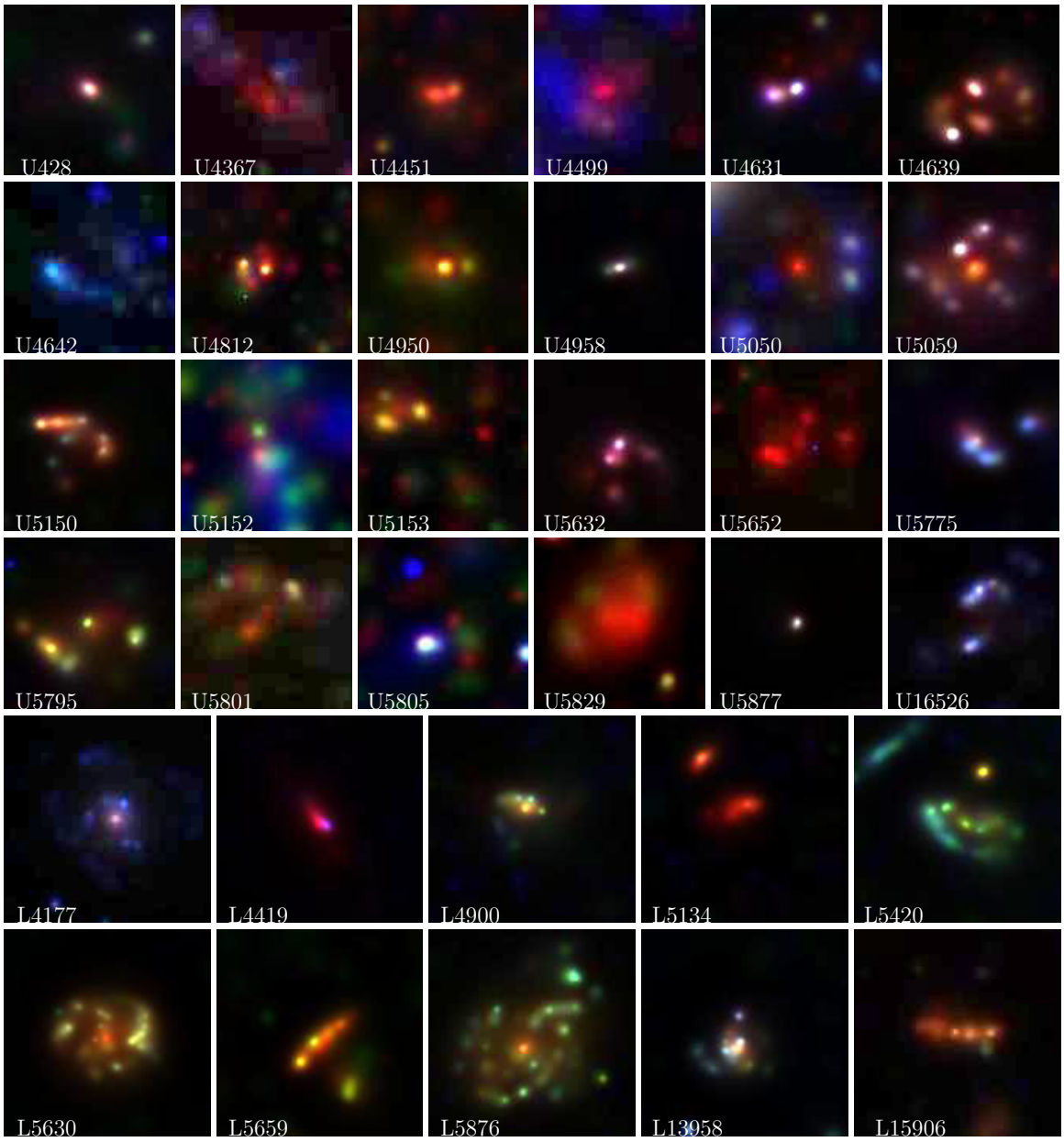

Figure 25. Three color images for 24 ULIRGs and 10 LIRGs of our sample with *F435W*, *F606W*, and *F850LP* ACS coverage. The field of view is $3'' \times 3''$ and $4'' \times 4''$ for ULIRGs and LIRGs, respectively. The composed image was obtained by giving the same weight to each band.

at the median redshift of 1.9 and 0.9, respectively. To obtain the three-color images, we filtered each ACS image with a wavelet transform to get rid of the background noise and to enhance the faint and extended morphological features. The technique used to filter the signal is a two-dimensional generalization of the method described in detail in Fadda et al. (1998). To each band we assigned the same weight.

Many extended sources, such as ULIRG4367, 4451, 5652, and 5829, are also very red, suggesting that dust obscuration could be in play. Only about four sources (428, 4950, 4958, 5877) have very compact or nearly unresolved morphologies. It is interesting to note that two of these compact morphology sources (ULIRG4958 and 5877) show very blue compact cores in Figure 25 and are AGN-dominated systems with weak or no PAH emission shown in Figure 7. This correspondence between the rest-frame optical compact morphologies and the mid-IR AGN-dominant spectra has also been found among a large sample of 24 μm selected ULIRGs in the *Spitzer* First Look Survey (Dasyra et al. 2008).

To better quantify morphological differences between our sample of galaxies and other galaxies in the field which are faint infrared emitters, we computed the Gini coefficient and M_{20} for the galaxies in our sample and control samples of faint infrared galaxies in the same redshift ranges. The Gini coefficient, G, is a statistic to measure the distribution of flux within the galaxy and M_{20} is the second-order moment of the brightest 20% of the galaxy's flux. These two nonparametric statistics have been introduced by Lotz et al. (2004) to quantify galaxy morphology. Normal galaxies form a sequence in the $G-M_{20}$ plot and, in the local universe, ULIRGs lie above this sequence. To compute these statistics, we followed the method described in Lotz et al. (2004) using our wavelet-filtered images to reduce the role of

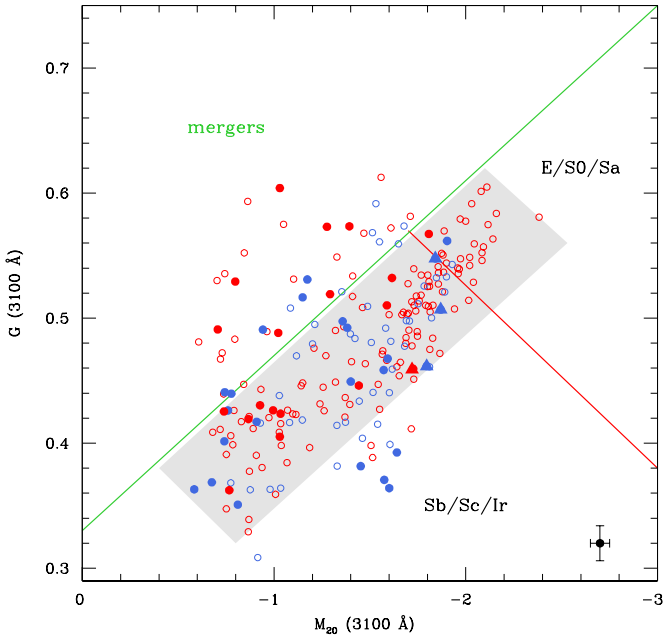

Figure 26. Gini coefficient and M_{20} statistic for the sample of LIRGs (red filled dots) at $z \sim 1$, ULIRGs (blue filled dots) at $z \sim 2$ and faint infrared sources in the redshift range $z \sim 1$ and $z \sim 2$ (red and blue open dots, respectively). The triangles correspond to the sources in our sample whose mid-IR emission is AGN-dominated. The gray shaded region highlights the Gini–M_{20} sequence which, locally, is populated by "normal" galaxies while local ULIRGs lie above the sequence. The three regions defined in Lotz et al. (2008) are marked with solid lines. The statistics have been computed from ACS images in the bands *F606W* and *F850LP* for galaxies at $z \sim 1$ and $z \sim 2$, respectively, to be approximately at the rest-frame wavelength of 3100 Å.

noise in the computation. We computed G and M_{20} using the *F850LP* and *F606W* images for ULIRGs at $z \sim 2$ and LIRGs at $z \sim 1$, respectively, to be roughly at the same 3100 Å rest-frame wavelength. We note that also the pixel size of the galaxies at $z \sim 1$ and $z \sim 2$ correspond to a similar physical scale (0.24 and 0.25 kpc, respectively, with our adopted cosmology), so that we can compare the values computed for the two redshift ranges. To compute the errors on the coefficients, we proceeded using Monte Carlo simulations. It is, in fact, impossible to have a direct error propagation since the computation of the coefficients involves filtering of the image, selection of regions, sorting of values, and search of source center. Therefore, for each source, we created 50 synthetic images by adding a random realization of a noise image (assuming a Gaussian distribution with dispersion equal to the rms of the image) to the wavelet-filtered image. After adding the original zero, we re-ran the code to measure the two coefficients on the synthetic images and estimated the errors assuming that they are equal to the dispersion of the values computed from the synthetic images. The measured errors are 0.014 ± 0.011 and 0.04 ± 0.04 for the G and M_{20} coefficients, respectively.

In Figure 26, we report the G and M_{20} values for the galaxies of our sample for which the signal-to-noise was sufficient to compute them and values for a control sample of galaxies with faint infrared emission (less than 20μJy at 24 μm) in the redshift ranges 0.8–1 and 1.8–2 where we find most of the galaxies of our sample. The typical 1σ error is reported in the lower right corner. A gray shaded region highlights the G–M_{20} sequence which, locally, is typically populated by "normal" galaxies while ULIRGs are found above that sequence. The three regions of the plot defined by Lotz et al. (2008) populated by merger, early-type, and late-type galaxies are marked with solid lines. The G–M_{20} sequence found by Lotz et al. (2008) in the Groth strip at $0.2 < z < 1.2$ in the rest-frame blue band is well reproduced by our study, although at a bluer rest-frame wavelength. We immediately note that the separation between infrared-active and infrared-quiet galaxies is not so clear as for normal and IR-luminous local galaxies. Most of the galaxies of our sample follow the same G–M_{20} sequence as the majority of the infrared-quiet galaxies. Lotz et al. (2008) found that the percentage of 24 μm sources at $0.4 < z < 1.0$ with $L_{\rm IR} > 10^{11}\,L_{\odot}$ are disk galaxies and only $\sim$15% are classified as major merger candidates. At the 3100 Å rest frame, our study shows that $z \sim 1$ LIRGs have a higher merger rate (37^{+22}_{-16}%) and that only 21^{+15}_{-10}% of the ULIRGs at $z \sim 2$ can be classified as mergers. We can therefore conclude that the morphologies of most of the IR-luminous galaxies at $z \sim 1$ and $z \sim 2$ do not differ in most of the cases from those of "normal" infrared-quiet galaxies. Repeating the analysis for the LIRGs of our sample in the blue rest frame, i.e., using the *F850LP* band ACS images, only two galaxies populate the "merger" region for a percentage of 10^{+14}_{-7}%, which is perfectly compatible with the results from Lotz et al. (2008). This result is not surprising since the rest-frame 3100 Å light is more sensitive to massive, young stars so that late-type galaxies appear more patchy and have no prominent optical bulge with respect to optical images (see, e.g., Kuchinski et al. 1999). In the case of ULIRGs, we have *HST* NICMOS images in the H band, approximately corresponding to the blue rest frame at $z \sim 1.9$, for a subset of 10 ULIRGs (see Figure 27). The Gini coefficients have a typical difference of 0.02 with respect those computed in the ACS images. All these sources are classified as "normal" galaxies in the G–M_{20} plot. Unfortunately, we do not have NICMOS coverage for the three ULIRGs which fall in the merger region of the G–M_{20} plot.

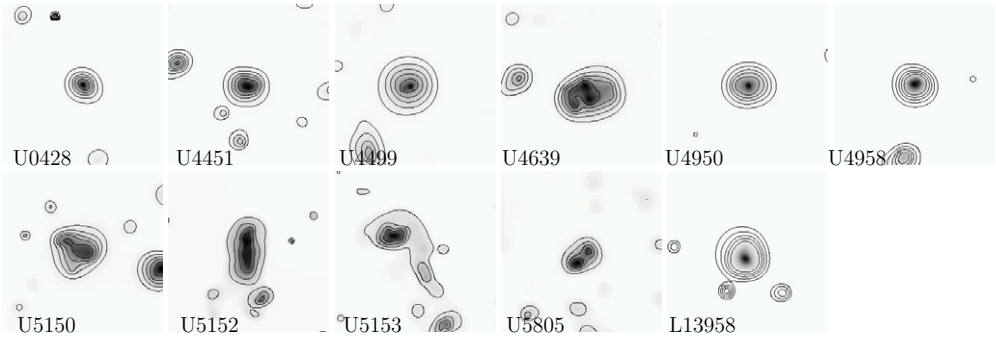

Figure 27. Plot shows the *HST*/NICMOS H-band $3'' \times 3''$ images centered on 10 ULIRGs and one LIRG of our sample. Labels correspond to the object IDs.

5. SUMMARY

The study presented in this paper aims to characterize the mid-IR spectral properties of very faint 24 μm sources with $S_{24\,\mu m} \sim 0.15$–0.45 mJy, specifically targeting LIRGs at $z \sim 1$ and ULIRGs at $z \sim 2$. This sample contains the faintest sources observed with IRS, reaching the limit of the instrument capability. These 24 μm faint LIRGs and ULIRGs are infrared luminous, sampling the typical luminosities of infrared luminosity functions at $z \sim 1$ and 2. Furthermore, they are similar to normal galaxies selected by optical/near-IR surveys in the sense that their stellar masses are $\lesssim M^*$, the turnover of the mass functions ($\sim 2 \times 10^{11}\,M_\odot$). The mid-IR spectra, in combination with X-ray, IR, and optical observations, have allowed us to determine physical properties of high-z LIRGs and ULIRGs, putting them in the context of larger galaxy populations selected at optical/near-IR wavelength. The major results of this work can be summarized as follows.

1. The vast majority of our sample (45 out of 48) has IRS spectra with clear PAH emission and/or silicate absorption, allowing secure redshift measurements. In particular, a third of the $z \sim 2$ ULIRGs are DRGs (galaxies with $(J - K) \gtrsim 2.3$) for which redshifts are very difficult to determine from optical or near-IR spectroscopy. Our finding of DRGs being dusty star forming galaxies, rather than passively evolving old stellar population is consistent with previous studies by (Labbé et al. 2005; Wuyts et al. 2007; Papovich et al. 2006).
2. The fraction of AGN harbored by the sources in our sample is much smaller than that of other samples of more luminous distant ULIRGs in the literature. From the analysis of our mid-IR sources, we estimate that their total IR emission is mainly powered by star formation. AGN emission dominates the energy output of LIRGs and ULIRGs only for 5% and 12% of them, respectively.
3. A quantitative analysis of the morphology based on ACS images reveals that most of the IR-luminous galaxies of our sample do not differ significantly from the majority of the IR-quiet galaxies at the same redshift range. At the 3100 Å rest frame, 37^{+22}_{-16}% of the $z \sim 1$ LIRGs and 21^{+15}_{-10}% of the $z \sim 2$ ULIRGs have Gini coefficients higher than those of normal IR-quiet galaxies. In the blue rest frame, 10^{+14}_{-7}% of the $z \sim 1$ LIRGs fall in the merger region of the Gini–M_{20} plot which is compatible with the 15% found by Lotz et al. (2008) among infrared galaxies with $L_{IR} > 10^{11}\,L_\odot$ at $0.4 < z < 1.0$.
4. We found a maximum value of ~ 1 μm for $EW_{6.2\,\mu m}$ for all infrared galaxies, independent of redshift and luminosity. This ceiling in 6.2 μm PAH strength is due to the fact that, for pure starbursts, the strength of the PAH line and of the underlying continuum are both proportional to the luminosity due to star-forming activity. At $L_{24\,\mu m} \gtrsim 10^{11}\,L_\odot$, there is a clear anti-correlation between the rest-frame 24 μm luminosity and 6.2 μm PAH EW. The 6.2 μm PAH EW of the $z \gtrsim 1$ sources is systematically greater than that of the local luminous galaxies in the same luminosity range. This is likely due to an AGN contribution in high-redshift galaxies lower than that of local IR luminous galaxies.
5. All our $z \sim 2$ ULIRGs are BzK galaxies with infrared excess, according to Daddi et al. (2004) definitions. Stacking all the sources whose infrared flux is not dominated by AGN emission, we provide quantitative constraints on the dust obscured AGN emission at the rest-frame 6 μm. By subtracting from the spectra around the 6.2 μm PAH feature the scaled averaged starburst spectrum, we measured the average AGN powered continuum at 6 μm, estimating an average intrinsic X-ray AGN luminosity of $L_{2-10\,keV} = (0.1 \pm 0.6) \times 10^{43}$ erg s^{-1}, a value substantially lower than that inferred from the X-ray stacking analysis in Daddi et al. (2007). A similar analysis on the LIRG sample suggests that their emission is mostly powered by star formation.

In conclusion, our mid-IR spectra of LIRGs and ULIRGs at $z \sim 1$ and 2 reveal that the majority of these galaxies have strong PAH emission and are starburst dominated. The Compton-thick AGN contribution to bolometric luminosity for this sample selected with $S_{24\,\mu m} \sim 0.15$–0.5 mJy is small. The so-called IR excess for these faint 24 μm selected ULIRGs at $z \sim 2$ is mainly due to the strong PAH contribution to the rest-frame mid-IR luminosity which leads to overestimations of L_{IR} and to underestimation of the UV dust extinction.

This research made use of Tiny Tim/*Spitzer*, developed by John Krist for the Spitzer Science Center. The Center is managed by the California Institute of Technology under a contract with NASA. We are grateful to Haojing Yan for providing us the reduced NICMOS *H*-band stamp images for some of our sources. We thank P. Capak for helpful discussions. We are grateful to the anonymous referee for the detailed reading of the paper and for many ideas and suggestions to improve the quality of the paper. Support for this work was provided by NASA through an award issued by JPL/Caltech. S. Wuyts acknowledges support from the W. M. Keck Foundation.

APPENDIX A

IRSLOW: A SOFTWARE PACKAGE FOR LOW-RESOLUTION IRS SPECTRA

For the analysis of the spectra presented in this paper, we developed a new software package called "IrsLow." This software allows one to exploit in an optimal way the redundancy of the data taken with the IRS spectrograph and to extract spectra in a very flexible way. The software and a tutorial are available online.[18] The code requires as input the BCD produced by the *Spitzer* pipeline and uses the full redundancy of the data to reject bad pixels and compute the residual background of the observations. Once the bad pixels are masked and the background subtracted from each individual image, it coadds all the images of each order at different positions. The parallel data of non-primary orders are coadded to identify and extract spectra of serendipitous sources. The spectra are extracted using PSF fitting and the code allows the simultaneous extraction of two spatially close spectra. An example output from this code is shown in Figure 28.

The optimal background subtraction is done iteratively with manually masking off all spectra. Uncertainty and background images are obtained from the stacked BCD after the rejection of pixels affected by cosmic rays or sources. A biweight estimator (Tukey 1958) is also used to compute robust estimates of average and dispersion with a low number (~ 10) of frames. After extracting the spectrum, each PSF fit for a single wavelength position can be visualized to delete other possible outliers and therefore improve the fit. Pixels with highly varying responsivity (i.e., rogue pixels in the IRS jargon) are identified by comparing

[18] http://web.ipac.caltech.edu/staff/fadda/IrsLow

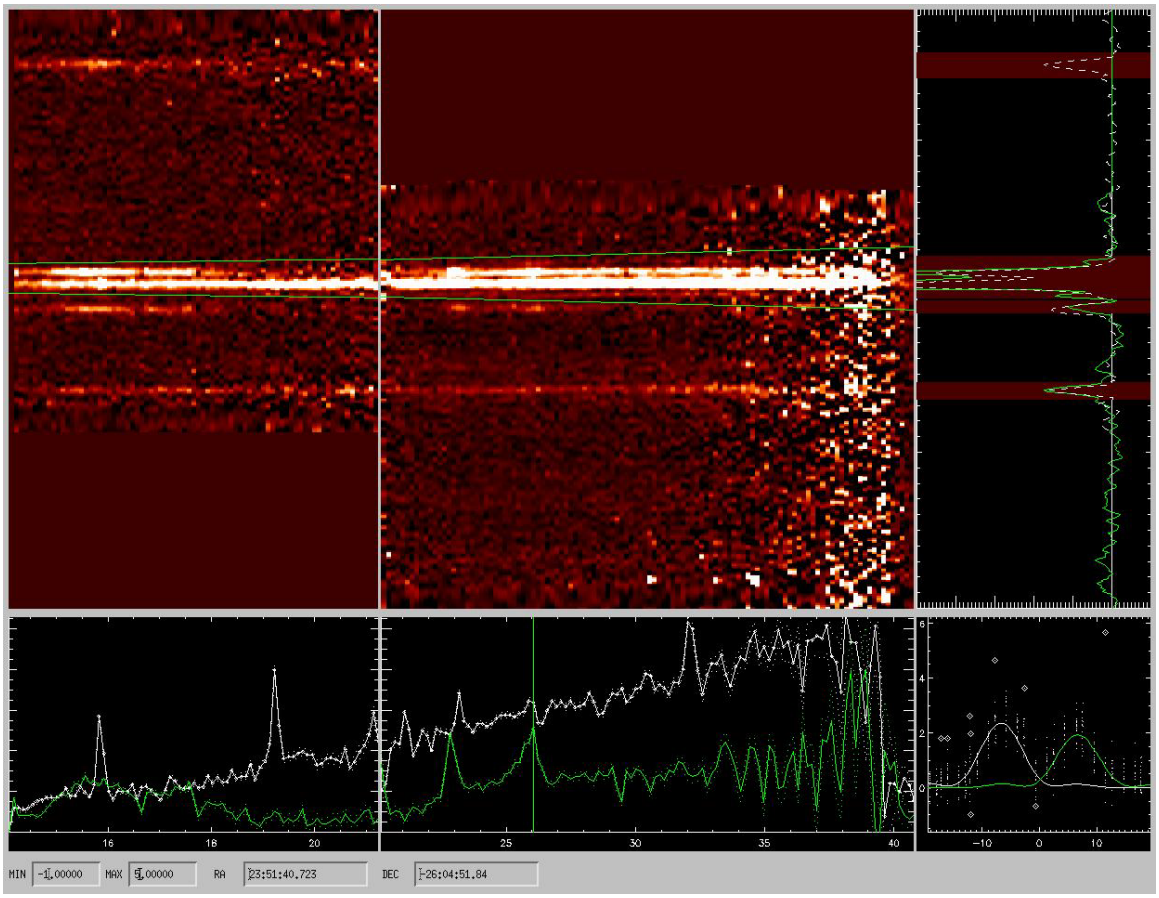

Figure 28. Analysis of an IRS observation through the GUI of the IrsLow code. In this case, the target is a double source. At least other three serendipitous sources are visible. The two images show the second and first orders after coadding all the frames (including the parallel observations). In the right upper panel, the profiles of the averaged rows of the two orders are displayed. The shaded regions have been masked to compute better background and rms images. Spectra of the two sources between the green lines on the images have been extracted and are shown in the lower left panels. Finally, the PSF spectral fit at the wavelength corresponding to the vertical line is shown in the right-bottom window. Each point corresponds to a pixel in the original frames. Circled points are masked for the fit. The lower boxes contains the limits of the image and coordinates of the extracted spectrum.

(A color version of this figure is available in the online journal.)

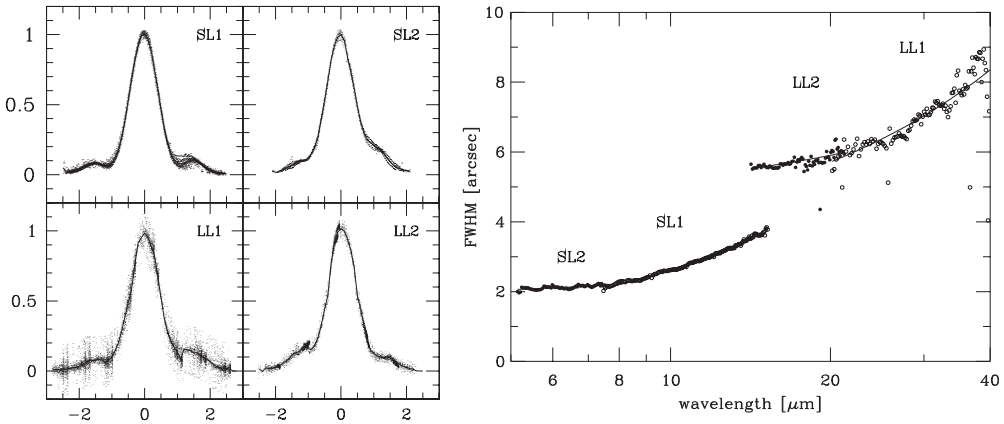

Figure 29. Spatial PSF profiles (left) and FWHM as a function of the wavelength (right) in the different orders computed with calibration stars. Amplitude and FWHM of the PSF profiles are normalized to one. These PSFs are used for the optimal extraction with IrsLow.

their rms values to those of the neighboring pixels. The final image is obtained by fitting a B spline at each wavelength to all the flux values from different pixels at their relative spatial positions. The fit is repeated three times, discarding 7σ and 4σ outliers in the second and third iterations, respectively. We derive PSF profiles using the IRS calibration stars. The average profiles are obtained by normalizing the flux of the spectra and scaling the FWHM as a function of the wavelength. The scaling of the FWHM is shown in Figure 29. Finally, the extracted spectra are saved in ASCII files with names equal to their spatial coordinates. The flux and wavelength calibration files are the same as those included in the IRS software SPICE. The calibration version is automatically selected by the software according to the information stored in the BCD headers. In fact,

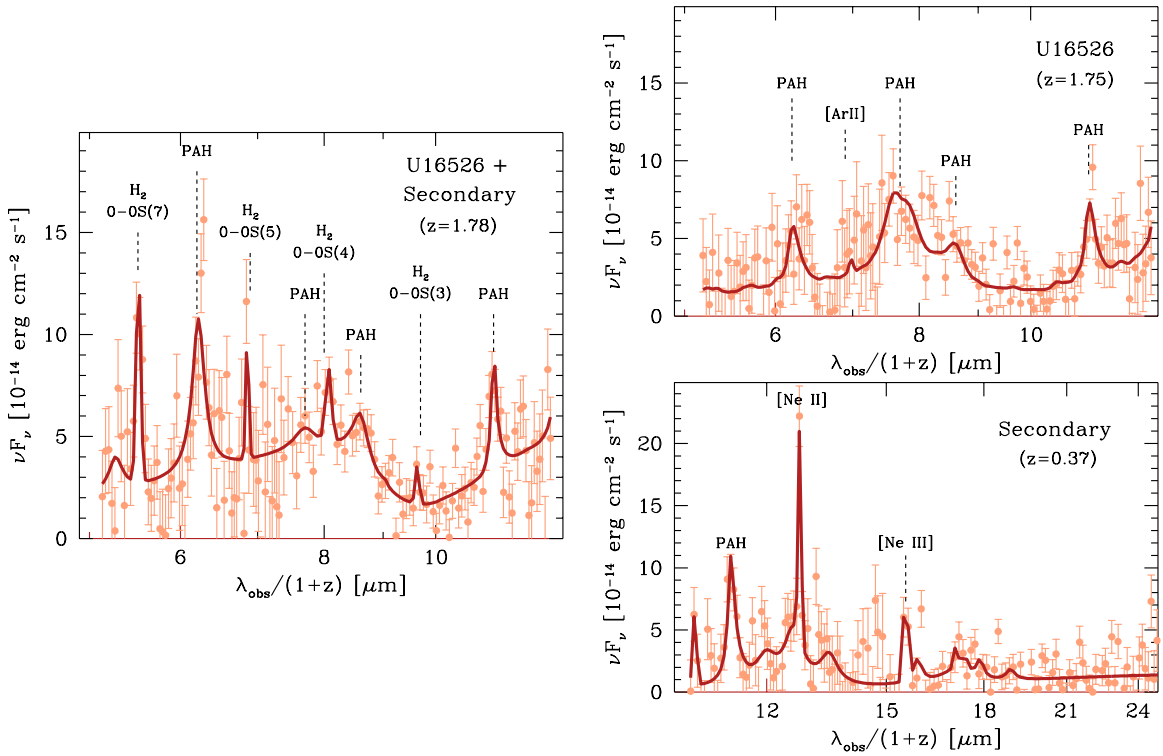

Figure 30. Spectral extraction of ULIRG 16526 considering one object (left) and fitting two objects (right). If only a single spectrum is extracted, spectral features from a nearby low-redshift object (at $z = 0.37$) could be wrongly interpreted as strong H_2 and 6.2 μm PAH features.
(A color version of this figure is available in the online journal.)

the calibration version is linked to the version of the pipeline used to obtain the BCD files.

One unique feature of our IRS reduction software is how it handles confused spectra from two close-by sources. As shown in Figure 28, the software allows the optimal extraction of two close sources at the same time by using our derived PSF profiles, shown in Figure 29. This feature has been particularly useful in the case of the source U16526. The observed IRS spectrum for U16526 is, in fact, a blend of two spectra at $z = 0.37$ and $z = 1.77$ (photometric redshifts from the FIREWORKS catalog), spatially separated by only 6″. This corresponds to the spatial resolution of the IRS spectrograph in the wavelength range used in the observation. When displaying this spectrum with our software, one can see only that the major features of the two sources are slightly spatially displaced although the continuum of the two sources is blended. In our first extraction, we erroneously considered one single source and interpreted some strong emission features as H_2 lines. Then, after examining the 24 μm image of the source, we realized that the spectrum was a blend of spectra from two different sources at different redshifts. The unique deblending capability of our software allowed us to separate the spectra of these two confused sources. In Figure 30, the left panel shows the total spectrum, which is the sum of two spectra, one at $z = 0.37$ and the other at $z = 1.75$, illustrated on the top right and bottom right, respectively. At this point, it was clear that the H_2 lines in the blended spectrum were in fact only strong emission features of the $z = 0.37$ source.

REFERENCES

Alexander, D. M., et al. 2003, AJ, 125, 383
Armus, L., et al. 2006, ApJ, 640, 204
Armus, L., et al. 2007, ApJ, 656, 148
Bauer, F., Yan, L., Sajina, A., & Alexander, D. 2010, ApJ, 710, 212
Bertin, E., & Arnouts, S. 1996, A&A, 117, 393
Bertincourt, B., et al. 2009, ApJ, 705, 68
Boquien, M., et al. 2009, ApJ, 706, 553
Brandl, B. R., et al. 2006, ApJ, 653, 1129
Bruzual, G., & Charlot, S. 2003, MNRAS, 344, 1000
Calzetti, D., et al. 2000, ApJ, 533, 682
Caputi, K. I., Dunlop, J. S., McLure, R. J., & Roche, N. D. 2004, MNRAS, 353, 30
Caputi, K. I., McLure, R. J., Dunlop, J. S., Cirasuolo, M., & Schael, A. M. 2006, MNRAS, 366, 609
Caputi, K. I., et al. 2007, ApJ, 660, 97
Chapman, S. C., Blain, A. W., Smail, I., & Ivison, R. J. 2005, ApJ, 622, 772
Chapin, E. L., Hughes, D. H., & Aretxaga, I. 2009, MNRAS, 393, 653
Chary, R., & Elbaz, D. 2001, ApJ, 556, 562
Cortese, L., et al. 2006, ApJ, 637, 242
Daddi, E., Cimatti, A., Renzini, A., Fontana, A., Mignoli, M., Pozzetti, L., Tozzi, P., & Zamorani, G. 2004, ApJ, 617, 746
Daddi, E., et al. 2007, ApJ, 670, 173
Dale, D. A., & Helou, G. 2002, ApJ, 576, 159
Dasyra, K. M., Yan, L., Helou, G., Surace, J., Sajina, A., & Colbert, J. 2008, ApJ, 680, 232
Desai, V., et al. 2007, ApJ, 669, 810
Diolaiti, E., et al. 2000, A&AS, 147, 335
Dole, H., et al. 2006, A&A, 451, 417
Elbaz, D., et al. 2002, A&A, 384, 848
Fadda, D., et al. 1998, A&AS, 127, 335
Fadda, D., et al. 2002, A&A, 383, 838
Fadda, D., et al. 2006, AJ, 131, 2859
Farrah, D., et al. 2008, ApJ, 677, 957
Fixsen, D. J. 1998, ApJ, 508, 123
Franceschini, A., et al. 2009, A&A, in press (arXiv:0906.4264F)
Franx, M., et al. 2003, ApJ, 587, L79
Gawiser, et al. 2006, ApJS, 162, 1
Genzel, R., et al. 1998, ApJ, 498, 579
Giavalisco, M., et al. 2004, ApJ, 600, 93
Greve, T. R., et al. 2005, MNRAS, 359, 1165
Houck, J. R., et al. 2004, ApJS, 154, 18
Ilbert, O., et al. 2010, ApJ, 709, 644
Kriek, M., et al. 2008, ApJ, 677, 219

Kroupa, P. 2001, MNRAS, 322, 231
Kuchinski, L. E., et al. 1999, ApJS, 131, 441
Labbé, I., et al. 2005, ApJ, 624, L81
Lagache, G., Puget, J.-L., & Dole, H. 2005, ARA&A, 43, 727
Lagache, G., et al. 2004, ApJS, 154, 112
Laurent, O., Mirabel, I. F., Charmandaris, V., Gallais, P., Madden, S. C., Sauvage, M., Vigroux, L., & Cesarsky, C. 2000, A&A, 359, 887
Lehmer, B. D., et al. 2005, ApJS, 161, 21
Le Fèvre, O., et al. 2004, A&A, 428, 1043
Le Floc'h, E, et al. 2005, ApJ, 632, 169
Lotz, J. M., Primack, J., & Madau, P. 2004, AJ, 128, 163
Lotz, J. M., et al. 2008, ApJ, 672, 177
Luo, B., et al. 2008, ApJS, 179, 19
Lutz, D., Spoon, H. W. W., Rigopoulou, D., Moorwood, A. F. M., & Genzel, R. 1998, ApJ, 505, L103
Lutz, D., et al. 1996, A&A, 315, L137
Lutz, D., et al. 2004, A&A, 418, 465
Magnelli, B., Elbaz, D., Chary, R. R., Dickinson, M., Le Borgne, D., Frayer, D. T., & Willmer, C. N. A. 2009, A&A, 496, 57
Marsden, G., et al. 2009, ApJ, 707, 1729
Menéndez-Delmestre, K., et al. 2007, ApJ, 655, L65
Meurer, G. R., Heckman, T. M., & Calzetti, D. 1999, ApJ, 521, 64
Meurer, G. R., Heckman, T. M., Leitherer, C., Kinney, A., Robert, C., & Garnett, D. R. 1995, AJ, 110, 2665
Mignoli, M., et al. 2005, A&A, 437, 883
Murphy, E. J., Chary, R.-R., Alexander, D. M., Dickinson, M., Magnelli, B., Morrison, G., Pope, A., & Teplitz, H. I. 2009, ApJ, 698, 1380
Papovich, C., et al. 2006, AJ, 132, 231
Pope, A., et al. 2008, ApJ, 675, 1171
Popesso, P., et al. 2009, A&A, 494, 443
Puget, J.-L., et al. 1996, A&A, 308, L5
Ranalli, P., Comastri, A., & Setti, G. 2003, A&A, 399, 39
Reddy, N. A., Steidel, C. C., Pettini, M., Adelberger, K. L., Shapley, A. E., Erb, D. K., & Dickinson, M. 2008, ApJS, 175, 48
Reddy, N. A., et al. 2006, ApJ, 653, 1004
Riecke, G., et al. 2009, ApJ, 692, 556
Rix, H.-W., et al. 2004, ApJS, 152, 163
Sajina, A., Yan, L., Armus, L., Choi, P., Fadda, D., Helou, G., & Spoon, H. 2007, ApJ, 664, 713
Sajina, A., et al. 2008, ApJ, 683, 659
Sanders, D. B., & Mirabel, I. F. 1996, ARA&A, 34, 749
Serjeant, S., et al. 2008, MNRAS, 386, 1907
Smith, J. D., et al. 2007, ApJ, 656, 770
Spoon, H. W. W., et al. 2004, ApJS, 154, 184
Spoon, H. W. W., et al. 2007, ApJ, 654, L49
Szokoly, G. P., et al. 2004, ApJS, 155, 271
Tacconi, L. J., et al. 2006, ApJ, 640, 228
Teplitz, H., et al. 2007, ApJ, 659, 941
Tukey, J. W. 1958, Ann. Math. Stat., 29, 614
Valiante, E., Lutz, D., Sturm, E., Genzel, R., & Chapin, E. 2009, ApJ, 701, 1814
Valiante, E., Lutz, D., Sturm, E., Genzel, R., Tacconi, L. J., Lehnert, M. D., & Baker, A. J. 2007, ApJ, 660, 1060
van Dokkum, P. G., et al. 2004, ApJ, 611, 703
Vanzella, E., et al. 2006, A&A, 454, 423
Vanzella, E., et al. 2008, A&A, 478, 83
Veilleux, S., Kim, D.-C., & Sanders, D. B. 2002, ApJS, 143, 315
Veilleux, S., et al. 2009, ApJS, 182, 628
Voit, G. M. 1992, MNRAS, 258, 841
Weedman, D. W., et al. 2006, ApJ, 651, 101
Wolf, C., et al. 2004, A&A, 421, 913
Wuyts, S., Franx, M., Cox, T. J., Hernquist, L., Hopkins, P. F., Robertson, B. E., & van Dokkum, P. G. 2009a, ApJ, 696, 348
Wuyts, S., et al. 2007, ApJ, 655, 51
Wuyts, S., et al. 2008, ApJ, 682, 985
Wuyts, S., et al. 2009b, ApJ, 700, 799
Wuyts, S., et al. 2009c, ApJ, 706, 885
Yan, L., McCarthy, P. J., Weymann, R. J., Malkan, M. A., Teplitz, H. I., Storrie-Lombardi, L. J., Smith, M., & Dressler, A. 2000, AJ, 120, 575
Yan, L., et al. 2005, ApJ, 628, 604
Yan, L., et al. 2007, ApJ, 658, 778